



저작자표시-비영리-변경금지 2.0 대한민국

이용자는 아래의 조건을 따르는 경우에 한하여 자유롭게

- 이 저작물을 복제, 배포, 전송, 전시, 공연 및 방송할 수 있습니다.

다음과 같은 조건을 따라야 합니다:



저작자표시. 귀하는 원저작자를 표시하여야 합니다.



비영리. 귀하는 이 저작물을 영리 목적으로 이용할 수 없습니다.



변경금지. 귀하는 이 저작물을 개작, 변형 또는 가공할 수 없습니다.

- 귀하는, 이 저작물의 재이용이나 배포의 경우, 이 저작물에 적용된 이용허락조건을 명확하게 나타내어야 합니다.
- 저작권자로부터 별도의 허가를 받으면 이러한 조건들은 적용되지 않습니다.

저작권법에 따른 이용자의 권리는 위의 내용에 의하여 영향을 받지 않습니다.

이것은 [이용허락규약\(Legal Code\)](#)을 이해하기 쉽게 요약한 것입니다.

[Disclaimer](#)

Ph.D. Dissertation of Science Education

Spatio-temporal surface mass redistribution
in Amazon and Greenland
recovered by satellite gravimetry

위성 중력계를 활용한 아마존과 그린랜드
표면 질량의 공간-시간적 재분포 연구

February 2016

Graduate School of Science Education
Seoul National University
Earth Science Major

Jooyoung Eom

Spatio-temporal surface mass redistribution
in Amazon and Greenland
recovered by satellite gravimetry

위성 중력계를 활용한 아마존과 그린랜드
표면 질량의 공간-시간적 재분포 연구

지도교수 서 기 원

이 논문을 교육학박사 학위논문으로 제출함

2015 년 11 월

서울대학교 대학원

과학교육과 지구과학전공

엄 주 영

엄 주 영의 교육학박사 학위논문을 인준함

2016 년 1 월

위 원 장 _____

부위원장 _____

위 원 _____

위 원 _____

위 원 _____

Abstract

The Gravity Recovery and Climate Experiment (GRACE) satellite mission has provided monthly geopotential fields since its launch in March 2002. The monthly geopotential variations are closely related with Earth's surface mass redistribution such as water transportations among oceans, atmosphere and land. Nominally, GRACE solutions exclude effects from tides, ocean dynamics and barometric pressure by incorporating geophysical models for them. However, those models are imperfect, and thus GRACE solutions include the residual gravity effects. Particularly, unmodeled gravity variations of sub-monthly or shorter time scale cause aliasing error, which produces peculiar longitudinal stripes. Therefore, difficulty in recovery of surface mass variations from GRACE lies in the error reduction with least signal loss, especially at sub-basin spatial scale.

In this dissertation, Empirical Orthogonal Functions (EOF) method is examined to separate signals associated with surface mass variation from GRACE errors in Amazon Basin and Greenland Icesheet (GrIS). Because the two regions are different climatologically and geographically, spatio-temporal variability of signal and error in GRACE are distinct. Therefore, it is necessary to modify EOF method for different features of signal and error in the two regions. In this study, we develop novel methods based on rotated EOF and extended EOF for Amazon and GrIS, respectively. In Amazon Basin, the river discharge is estimated using water mass variation on the main stem. To achieve this, the terrestrial water storage (TWS) changes confined to the main stem have to be extracted not only from the

GRACE error, but also from TWS variations adjacent to the main stem. In Greenland, detail month-to-month ice mass variations are estimated based on from separation between signal and aliasing error.

The rotated EOF method over the Óbidos sub-basin successfully estimates river discharge in the basin. The resulting time series represents relative river discharge variations consistent to in-situ discharge estimate. However, the estimates are generally larger than in-situ data in high water seasons. This is likely due to detoured water in river pathway developed during flooding while GRACE observes integrated water mass variations in river channels. The rotated EOF method is extended to the entire Amazon Basin based on the results for Óbidos sub-basin. Therefore, the method provides total river discharge of Amazon basin, which has been unknown since in-situ observations are not available at the mouth of basin.

The extended EOF provides higher temporal and spatial ice mass variations in GrIS, and this method is superior to the spatial filtering conventionally used in this region. In particular, results of extended EOF remarkably agree with surface mass balance (SMB) outputs of regional climate model during winter season when SMB is a major contributor to mass changes in GrIS. On the base of this consistency, GRACE observations and the regional climate model are used to retrieve ice discharge near the coastal region. The GRACE-based ice discharge remarkably agrees with results independently obtained from ice thickness and velocity survey in amplitude and spatial distribution.

Keywords: GRACE, EOF, Amazon, Greenland, River discharge, Ice mass variation

Student Number: 2007-30920

Contents

Abstract	i
Chapter 1 Introduction	1
Chapter 2 Background	4
2.1 Connection between geoid and surface mass distribution .	4
2.1.1 Gravitational potential perturbation	5
2.1.2 Spherical harmonics	7
2.1.3 Useful relations for spherical harmonics	8
2.1.4 Recovering surface mass changes from GRACE data	12
2.2 Empirical Orthogonal Functions	14
2.2.1 Eigendecomposition	14
2.2.2 Singular Value Decomposition	17
Chapter 3 Amazon River discharge estimates	20
3.1 Introduction	20
3.2 Data and Method	25
3.2.1 In-situ data for river discharge	25
3.2.2 GRACE monthly gravity solutions	25
3.2.3 Rotated EOF method	26
3.2.4 Synthetic GRACE data	29
3.3 Results	33
3.3.1 Recovering river discharge from the synthetic data	33

3.3.2	Recovering river discharge from the real GRACE solutions	38
3.4	Discussion	50
Chapter 4	De-correlation of GRACE data on the GrIS	53
4.1	Introduction	53
4.2	Data and Method	56
4.2.1	Monthly GRACE solutions	56
4.2.2	Extended EOF	57
4.3	Results	61
4.4	Discussion	75
Chapter 5	Conclusions	80
	국문요약	99

List of Figures

Figure 3.1	Degree amplitudes for real and synthetic GRACE data.	32
Figure 3.2	EOF results for the synthetic GRACE data . . .	34
Figure 3.3	REOF results for the synthetic GRACE data . .	37
Figure 3.4	REOF time series for the synthetic GRACE data at the basin mouth of Amazon	39
Figure 3.5	EOF results for the real GRACE data	41
Figure 3.6	REOF results for the real GRACE data	42
Figure 3.7	MODIS images around the Óbidos station	45
Figure 3.8	Comparisons of <i>RPC1</i> with WBE and In-situ . .	46
Figure 3.9	Regression results between WBE and <i>RPC1</i> . . .	48
Figure 3.10	Total discharge estimates for the Amazon Basin .	51
Figure 4.1	The hovmöller diagrams for filtered and unfiltered GRACE data	63
Figure 4.2	Hovmöller diagrams of EEOF spatial modes for SH coefficients	65
Figure 4.3	The hovmöller diagrams for EEOF filtered GRACE data	67
Figure 4.4	Basin average estimations with and without de-correlation filter and EEOF	69

Figure 4.5	Comparisons of SMB fields and month-to-month GRACE observations	72
Figure 4.6	Mean monthly difference maps of ice mass	74
Figure 4.7	Ice discharge map of GrIS recovered from GRACE	76
Figure 4.8	Locations and amplitude of 178 marine-terminating outlet glaciers.	77

Chapter 1. Introduction

Understanding of the global water cycle, the transportation of water among oceans, atmosphere and land, is essential to understand Earth's climate and its change. Water mass redistribution occurs via precipitation, evapotranspiration and surface/subsurface flow. Continuous observations for the meteorologic and hydrologic phenomena associated with water cycle are particularly important to predict climate changes and manage corresponding hazards. However, sparse ground in-situ stations hinder understanding the meteorologic and hydrologic process, and this problem is particularly true for remote area.

The gravity observation from space can be an alternative observation of water cycle because the redistribution of water mass alters the Earth's gravity field [*Cazenave and Chen, 2010*]. A dedicated-gravity satellite mission named 'Gravity Recovery and Climate Experiment (GRACE)' was launched in March 2002, and it has provided the Earth's gravity field every 30 days with unprecedented accuracy. The GRACE consists of two co-orbiting satellites 220 *km* apart at approximately 450 *km* altitude and measures the distance between them by on-board microwave ranging system. The changes of inter-satellites range are used to map the gravity field with accuracy of 1 *cm* equivalent water height, which is about 2 orders of magnitude better than those of EGM96, the pre-GRACE gravity model. Since its launch, the monthly gravity anomalies provided by GRACE are

widely used in hydrologic, atmospheric, oceanographic and cryospheric researches with global to regional scale. However, its applications for smaller spatial scale less than a few hundreds kilometers are limited due to errors from various sources such as random noise and aliasing.

The aliasing error is a unique uncertainty in GRACE gravity solutions. Monthly global gravity solutions from GRACE are estimated based on along-track inter-satellites observations during a given month. Therefore any shorter time-varying gravity effect than a month causes aliasing error in the gravity solutions. To reduce the aliasing error, numerical models (tides, atmospheric surface pressure and ocean bottom pressure) are incorporated to remove the higher frequency effect. However, the model predictions are not perfect, and thus residual higher temporal gravity variations contaminate monthly gravity solutions. The aliasing error is particularly severe at GRACE orbit resonant orders of spherical harmonics (SH) [Seo *et al.*, 2008] and consequently shows peculiar north-south longitudinal stripes pattern in grids, which is equivalent to correlated variations of SH even (or odd) degree coefficients around resonant orders.

To suppress random noise and aliasing error, two filtering procedures are commonly used in GRACE studies. The north-south stripe patterns are removed by de-correlation filter [Swenson and Wahr, 2006]. After the de-correlation procedures, a portion of longitudinal stripes and random noise are still remained in gridded water mass redistribution. The residual errors can be suppressed by Gaussian spatial averaging that diminishes high SH degree and order contributions of GRACE data [Wahr *et al.*, 1998]. Gridded water mass redistribution after the conventional two-step

filters shows much broader spatial features than that of unfiltered data. This indicates that GRACE data filtering leads to attenuations of signals, which prohibits examining sub-basin scale studies [*Chen et al.*, 2007, 2011].

To recover the signal attenuation, several approaches have been developed. *Velicogna and Wahr* [2005] estimated mass change in the Greenland by the scaled averaging function to compensate the signal loss into nearby oceans (leakage effect). This method assumes a uniform mass distribution in a study region. Therefore, recovered signal is subject to be biased due to high spatial variability of water mass [*Longuevergne et al.*, 2010]. More recently, *Chen et al.* [2013] used forward modeling method to avoid signal leakage into the ocean with assumption that the oceanic signal near coastal regions is occurred from signal smoothing over land. This method has been successfully applied to examine basin-averaged water (or ice) mass variations. However, it still has limitation to interpret detail spatial pattern of land signal.

As an alternative method, the empirical orthogonal function (EOF) analysis is examined to enhance the signal recovery and spatial pattern of GRACE data. In this dissertation, EOF method is applied for Amazon River discharge (Chapter 3) and Greenland ice mass variations (Chapter 4). Basic mathematical concepts for GRACE data processing and EOF are introduced in Chapter 2, and more specific methods that are appropriate for the two studies are explained at Method sub-sections of Chapters 3 and 4. Concluding remarks and discussion are made in Chapter 5.

Chapter 2. Background

In this chapter, geophysical concepts and mathematical formulas to understand EOF application of GRACE data are introduced. The first section of this chapter explains the relationship between surface mass variations and changes in geoid. Global gravity model observed by GRACE is represented by geopotential spherical harmonics (SH). Detail mathematical procedures to estimate surface mass variations from geopotential SH coefficients are derived. The second part of this chapter includes singular value decomposition (SVD) for EOF analysis, which is a fundamental data processing tool in this dissertation. Although modified EOFs are used for Amazon River discharge (Chapter 3) and Greenland ice mass variations (Chapter 4), those EOFs share principal ideas with the SVD.

2.1 Connection between geoid and surface mass distribution

The monthly geoid changes observed from GRACE are caused by redistributions of mass in the Earth. During GRACE operational period, any mass change occurring at cores and lower mantle is not expected [*Dickey et al.*, 1997]. This indicates that geoid height variations observed by GRACE is associated with mass variations occurring at the outermost thin layer including uppermost mantle, crust, atmosphere, hydrosphere and cryosphere [*Wahr et al.*, 1998].

In addition, gravity effects from atmospheric and barotropic ocean mass redistribution and tides are corrected using numerical models [Betadpur, 2012] during GRACE data processing. Therefore, nominally, GRACE gravity solutions include gravity variations associated with water and ice mass redistributions, post-glacial rebound (PGR) and co- and post-seismic deformation [Dickey *et al.*, 1997].

In following subsections, the relationship between GRACE solutions and surface mass distributions is derived. The derivations are made on SH domain, since GRACE gravity solutions are provided by SH coefficients representing global geoid variations. Gravitational perturbation resulting from a point mass on a sphere can be represented by Legendre polynomial. The potential change associated with a point mass is extended into geopotential variations for global surface mass redistribution. Finally, the geopotential changes perturbed by surface mass redistribution are compared with geoid variations observed by GRACE. This comparison is useful to recover surface mass variations from GRACE observations.

2.1.1 Gravitational potential perturbation

The perturbation of gravitational potential at $\mathbf{r}(r, \theta, \phi)$ produced by a point unit mass located on a sphere with radius a , $\mathbf{r}'(a, \theta', \phi')$ gives

$$\Psi(\mathbf{r}) = \Psi(r, \gamma) = \frac{a^2 g}{M_e} \frac{1}{\sqrt{a^2 + r^2 - 2ar \cos \gamma}}, \quad (2.1)$$

where γ measures an angular distance between observation point r , and a point unit mass r' . M_e and g are the mass and gravity acceleration of the Earth, respectively. Equation (2.1) is the generating function for the

Legendre polynomials, and the equation can be expanded as follow:

$$\frac{a^2 g}{M_e r} \left[1 + \left(\frac{a}{r} \right)^2 - 2 \frac{a}{r} \cos \gamma \right]^{-1/2} = \frac{a^2 g}{M_e} \sum_{l=0}^{\infty} \frac{a^l}{r^{l+1}} P_l(\cos \gamma), \quad r \geq a, \quad (2.2)$$

where $P_l(\cos \gamma)$ represent Legendre polynomials of l th degree in $\cos \gamma$.

Equation (2.2) describes the gravitational potential perturbation associated with a point mass. This point mass loaded on the Earth also deforms the underlying surface. The elastic response of the Earth produces additional gravitational perturbation. To consider this effect, each Legendre degree l term in equation (2.2) needs to include the elastic response with appropriate boundary conditions [Farrell and Clark, 1976]. Since this study focuses on gravity variations during GRACE era (~ 15 -20 years), Earth's viscous response to a point load can be negligible, and then

$$\Psi^E(a, \gamma) = \Psi^E(\theta, \phi | \theta', \phi') = \frac{ag}{M_e} \sum_{l=0}^{\infty} (1 + k_l) P_l(\cos \gamma), \quad (2.3)$$

where k_l is the load Love number of degree l [Farrell, 1972].

Ψ^E in equation (2.3) represents gravitational potential that is caused by a point mass on the Earth's surface and its elastic response of the Earth. Gravitational potential perturbation associated with continuous distribution of surface mass density changes, $\Delta \sigma(\theta', \phi')$, is calculated by via:

$$\Delta V(\theta, \phi) = \int_{\text{Earth surface}} \Psi^E(\theta, \phi | \theta', \phi') \Delta \sigma(\theta', \phi') d\Omega'. \quad (2.4)$$

This equation is a 2-dimensional convolution of surface density change ($\Delta \sigma$) and a point mass gravitational potential (Ψ^E) defined on the sphere. Global gravitational potential perturbation (ΔV) can be calculated via

repeated global integrations in equation (2.4), but it requires much computational time. Convolution in frequency domain (SH domain) can be an alternative to reduce computational time.

2.1.2 Spherical harmonics

The geoid is an equipotential surface of the Earth gravity field that coincides with mean sea level over the oceans. The shape of geoid N is conventionally represented by a sum of spherical harmonics [Kaula, 1966].

$$N(\theta, \phi) = a \sum_{l=0}^{\infty} \sum_{m=-l}^l N_{lm} \tilde{Y}_{lm}(\theta, \phi), \quad (2.5)$$

where a is the radius of the Earth, θ and ϕ are colatitude and east longitude, respectively. \tilde{Y}_{lm} are normalized spherical harmonics to lump the θ and ϕ dependence together into a single set of functions. To achieve normalization of the integrated squared polynomial over the unit sphere, each polynomial is multiplied by a normalizing function. In geodesy, it is common to use *fully normalization* and then \tilde{Y}_{lm} is defined by

$$\tilde{Y}_{lm}(\theta, \phi) = \sqrt{(2 - \delta_{m0})(2l + 1) \frac{(l - |m|)!}{(l + |m|)!}} P_{l|m|}(\cos\theta) \begin{cases} \cos m\phi, & m \geq 0 \\ \sin |m|\phi, & m < 0 \end{cases}, \quad (2.6)$$

where the P_{lm} are associated Legendre function and obtained by m times differentiating $P_l(x)$ with respect to x : $P_{lm}(x) = (1-x^2)^{(m/2)} d^m/dx^m P_l(x)$. As an alternative of equation (2.5), the following form is also used to separately denote the coefficients for cosine and sine.

$$N(\theta, \phi) = a \sum_{l=0}^{\infty} \sum_{m=0}^l \tilde{P}_{lm}(\theta) \{C_{lm} \cos(m\phi) + S_{lm} \sin(m\phi)\}, \quad (2.7)$$

where \tilde{P}_{lm} are the normalized associated Legendre functions,

$$\tilde{P}_{lm} = \sqrt{(2 - \delta_{m0})(2l + 1)} \frac{(l - |m|)!}{(l + |m|)!} P_{lm}(\cos\theta). \quad (2.8)$$

Here, C_{lm} and S_{lm} are known as Stoke's coefficients that are conventionally used to describe a satellite geoid model. N_{lm} in equation (2.5) comprise the Stoke's coefficients, but have a different configuration as follow:

$$N_{lm} = \begin{cases} C_{lm}, & m \geq 0 \\ S_{l|m|}, & m < 0. \end{cases} \quad (2.9)$$

2.1.3 Useful relations for spherical harmonics

The completeness of the spherical harmonics

The normalization factor in equation (2.6) has been chosen to make the spherical harmonics normalized to 4π . Squaring these functions and integrating over the sphere gives

$$\int_{\text{unit sphere}} \tilde{Y}_{lm}(\theta, \phi) \tilde{Y}_{kn}(\theta, \phi) d\Omega = 4\pi \delta_{lk} \delta_{mn}, \quad (2.10)$$

where $d\Omega = \sin\theta d\theta d\phi$ is the differential solid angle in spherical harmonics coordinates. Equation (2.10) shows that these functions are orthogonal and complete. This means that the spherical harmonics are linearly independent and implied that any function defined on the sphere can be expressed as

$$f(\theta, \phi) = \sum_{l=0}^{\infty} \sum_{m=-l}^l f_{lm} \tilde{Y}_{lm}(\theta, \phi). \quad (2.11)$$

Using equation (2.10), the spherical harmonic coefficients f_{lm} for $f(\theta, \phi)$ of the summation in equation (2.11) are given by

$$f_{lm} = \frac{1}{4\pi} \int f(\theta, \phi) \tilde{Y}_{lm}(\theta, \phi) d\Omega. \quad (2.12)$$

The reciprocal-distance formula

In several problems of geophysics, it is necessary to generalize the spherical harmonic addition theorem. Here proving of the theorem is suggested by simple derivation of spherical harmonics.

Consider two distinct points $r(\theta, \phi)$ and $r'(\theta', \phi')$ on a unit sphere in xyz -coordinate system and γ is an angle between them. Consider rotated $x'y'z'$ -coordinate system in which the z' -axis go through the $r'(\theta', \phi')$. This rotation of the coordinate system transforms a coordinate of $r(\theta, \phi)$ into $r(\gamma, \beta)$. γ is the polar angle with respect to z' -axis, and azimuthal angle, β , depends on direction of the x' - and y' -axes. In this coordinate system, equation (2.6) yields the following useful relation,

$$\tilde{Y}_{l0}(\gamma, \beta) = \sqrt{2l+1} P_l(\cos\gamma), \quad (2.13)$$

which links the Legendre functions to the spherical harmonics with $m = 0$. Since γ is determined by the relative distance between r and r' and the latter is fixed in this coordinate system, $P_l(\cos\gamma)$ in equation (2.13) can also be expanded in a Laplace series,

$$P_l(\cos\gamma) = \sum_{m=-l}^l p_m(\theta', \phi') \tilde{Y}_{lm}(\theta, \phi), \quad (2.14)$$

where the coefficients p_m depend on the fixed parameters θ' and ϕ' and can be solved by orthogonality of $\tilde{Y}_{lm}(\theta, \phi)$, i.e., equation (2.10),

$$p_m = \frac{1}{4\pi} \int P_l(\cos\gamma) \tilde{Y}_{lm}(\theta, \phi) d\Omega(\theta, \phi). \quad (2.15)$$

Note that $\int d\Omega(\theta, \phi)$ in equation (2.15) represents that the integration is carried in the xyz -coordinate system. In similar way to equation (2.14), $\tilde{Y}_{lm}(\theta, \phi)$ are also expanded by

$$\tilde{Y}_{lm}(\theta, \phi) = \sum_{n=-l}^l y_{mn}(\theta', \phi') \tilde{Y}_{ln}(\gamma, \beta), \quad (2.16)$$

where a new dummy index n is adopted to avoid confusion with the fixed index m . The spherical harmonic coefficients for $\tilde{Y}_{lm}(\gamma, \beta)$ are

$$y_{mn} = \frac{1}{4\pi} \int \tilde{Y}_{lm}(\theta, \phi) \tilde{Y}_{ln}(\gamma, \beta) d\Omega(\gamma, \beta),$$

where $d\Omega(\gamma, \beta)$ indicates the differential solid angle in the $x'y'z'$ -coordinate system. Inserting $n = 0$ and using equation (2.13) yield

$$y_{m0} = \frac{\sqrt{2l+1}}{4\pi} \int \tilde{Y}_{lm}(\theta, \phi) P_l(\cos\gamma) d\Omega(\gamma, \beta). \quad (2.17)$$

Because $d\Omega$ is the infinitesimal surface area on unit sphere, the rotation of coordinate system doesn't change this area and results of integration over the entire sphere, i.e. $d\Omega(\gamma, \beta)$ in equation (2.17) can be substituted by $d\Omega(\theta, \phi)$. This replacement allows inserting equation (2.15) into equation (2.17) and gives

$$y_{m0} = \sqrt{2l+1} p_m. \quad (2.18)$$

As γ approaches 0, r and r' become closer sufficiently, and thus equation (2.16) can be writes as follow:

$$\lim_{\gamma \rightarrow 0} \tilde{Y}_{lm}(\theta, \phi) = \tilde{Y}_{lm}(\theta', \phi') = \sum_{n=-l}^l y_{mn}(\theta', \phi') \tilde{Y}_{ln}(0, \beta). \quad (2.19)$$

Because $P_{lm}(\cos 0) = \delta_{m0}$, only the $n = 0$ term of the summation in equation (2.19) survives. Plugging of equation (2.18) into equation (2.19)

yields

$$\tilde{Y}_{lm}(\theta', \phi') = \sqrt{2l+1}y_{m0} = (2l+1)p_m, \quad (2.20)$$

and Legendre addition theorem is obtained by inserting equation (2.20) into equation (2.14) as follow:

$$P_l(\cos\gamma) = \frac{1}{2l+1} \sum_{m=-l}^l \tilde{Y}_{lm}(\theta, \phi) \tilde{Y}_{lm}(\theta', \phi'). \quad (2.21)$$

Convolution on the unit sphere

The convolution is defined on unit sphere as

$$f * h \equiv \int_{\text{unit sphere}} f(\theta, \phi | \theta', \phi') h(\theta', \phi') d\Omega', \quad (2.22)$$

where $d\Omega$ is a infinitesimal surface area, $\sin\theta d\theta d\phi$. The expansion of two integrands in equation (2.22) into spherical harmonics makes the computation of convolution to be simple. When one of the integrands is a longitude-independent function (i.e., zonal harmonics) such as equation (2.3), equation (2.22) is expressed as follow:

$$\int f(\gamma) h(\theta', \phi') d\Omega' = \int \sum_{l=0}^{\infty} f_l P_l(\cos\gamma) \sum_{k=0}^{\infty} \sum_{n=-k}^k h_{kn} \tilde{Y}_{kn}(\theta', \phi') d\Omega'.$$

Substituting equation (2.21) for $P_l(\cos\gamma)$ in first summation of above equation and using the orthogonality of \tilde{Y}_{lm} give,

$$\begin{aligned} f * h &= \sum_{l=0}^{\infty} \sum_{m=-l}^l \frac{f_l}{2l+1} \tilde{Y}_{lm}(\theta, \phi) \int \tilde{Y}_{lm}(\theta', \phi') \sum_{k=0}^{\infty} \sum_{n=-k}^k h_{kn} \tilde{Y}_{kn}(\theta', \phi') d\Omega' \\ &= 4\pi \sum_{l=0}^{\infty} \sum_{m=-l}^l \frac{f_l h_{lm}}{2l+1} \tilde{Y}_{lm}(\theta, \phi). \end{aligned} \quad (2.23)$$

2.1.4 Recovering surface mass changes from GRACE data

Changes in surface mass density defined on the Earth's surface can be also expanded using equation (2.11) as follow:

$$\Delta\sigma(\theta, \phi) = a \sum_{l=0}^{\infty} \sum_{m=-l}^l \Delta\sigma_{lm} \tilde{Y}_{lm}, \quad (2.24)$$

where $\Delta\sigma_{lm}$ are mass coefficients in representation of *fully normalization*. To find geopotential changes $\Delta V(\theta, \phi)$, at the Earth surface, equation (2.4) is used and the convolution is conducted by equation (2.23) with a infinitesimal surface area of Earth, $d\Omega = a^2 \sin\theta d\theta d\phi$.

$$\begin{aligned} \Delta V(\theta, \phi) &= a^2 \Psi^E * \Delta\sigma \\ &= 4\pi a^3 \frac{ag}{M_e} \sum_{l=0}^{\infty} \sum_{m=-l}^l \frac{1+k_l}{2l+1} \Delta\sigma_{lm} \tilde{Y}_{lm}(\theta, \phi). \end{aligned}$$

These geopotential changes are expressed alternatively using equation (2.8) for comparison with GRACE Stokes coefficients.

$$\Delta V(\theta, \phi) = ag \frac{3}{\rho_e} \sum_{l=0}^{\infty} \sum_{m=0}^l \frac{1+k_l}{2l+1} \tilde{P}_{lm}(\cos\theta) \{ \Delta \hat{C}_{lm} \cos(m\phi) + \Delta \hat{S}_{lm} \sin(m\phi) \}, \quad (2.25)$$

where ρ_e is Earth's average density given by $4\pi a^3/M_e$. \hat{C}_{lm} and \hat{S}_{lm} in the bracket of equation (2.25) are mass coefficients equivalent to $\Delta\sigma_{lm}$ in equation (2.24) (see, equation (2.9)).

The geopotential changes are also obtained from the GRACE Stoke's coefficients representing geoid height. From equation (2.7), changes in geoid are described by changes in each Stoke's coefficients,

$$\Delta N(\theta, \phi) = a \sum_{l=0}^{\infty} \sum_{m=0}^l \tilde{P}_{lm}(\cos\theta) \{ \Delta C_{lm} \cos(m\phi) + \Delta S_{lm} \sin(m\phi) \}. \quad (2.26)$$

Because $\Delta N/a \ll 1$, it is satisfied ΔV is equal to $g\Delta N$ at $r = a$ in a sufficient accuracy. Therefore, changes in geopotential can be described by changes in geoid height by multiplying gravity acceleration of Earth as follow:

$$\Delta V(\theta, \phi) = ag \sum_{l=0}^{\infty} \sum_{m=0}^l \tilde{P}_{lm}(\cos\theta) \{ \Delta C_{lm} \cos(m\phi) + \Delta S_{lm} \sin(m\phi) \}. \quad (2.27)$$

Comparing equation (2.25) and equation (2.27) yields the relation between mass coefficients and GRACE Stokes coefficients as follow:

$$\begin{Bmatrix} \Delta \hat{C}_{lm} \\ \Delta \hat{S}_{lm} \end{Bmatrix} = \frac{\rho_e}{3} \frac{2l+1}{1+k_l} \begin{Bmatrix} \Delta C_{lm} \\ \Delta S_{lm} \end{Bmatrix}, \quad (2.28)$$

which can be used to find the change in surface mass density from changes in geoid provided by GRACE Stokes coefficients, ΔC_{lm} and ΔS_{lm} , which gives

$$\Delta \sigma(\theta, \phi) = \frac{a\rho_e}{3} \sum_{l=0}^{\infty} \sum_{m=0}^l \tilde{P}_{lm}(\cos\theta) \frac{2l+1}{1+k_l} \{ \Delta C_{lm} \cos(m\phi) + \Delta S_{lm} \sin(m\phi) \}. \quad (2.29)$$

On the other hand, the change in the geoid can be calculated from the change in surface mass density as follow:

$$\Delta N(\theta, \phi) = \frac{3a}{\rho_e} \sum_{l=0}^{\infty} \sum_{m=0}^l \tilde{P}_{lm}(\cos\theta) \frac{1+k_l}{2l+1} \{ \Delta \hat{C}_{lm} \cos(m\phi) + \Delta \hat{S}_{lm} \sin(m\phi) \}. \quad (2.30)$$

2.2 Empirical Orthogonal Functions

Geophysical data are usually multivariate field in space-time domain. Empirical Orthogonal Functions (EOF), also known as Principal Component Analysis (PCA), is an appropriate technique to interpret geophysical data. EOF separates geophysical data set into spatial and temporal modes, and each mode is determined to maximize variance of a corresponding mode. In this dissertation, Rotated EOF (REOF) and Extended EOF (EEOF) methods are applied for Amazon River discharge (Chapter 3) and Greenland ice mass variations (Chapter 4), respectively. REOF and EEOF are modified EOF, and thus EOF is a fundamental data processing procedure in this study. Geophysical data decomposition into temporal and spatial modes is facilitated by diagonalization of data matrix based on Singular Value Decomposition (SVD). Since SVD is a generalized method of eigendecomposition, which decomposes only a square matrix, it is useful to understand eigendecomposition first.

2.2.1 Eigendecomposition

Some geophysical data properties can be easily understood when they are interpreted in a geometrical frame. Important spatial pattern of the data and its variance can be determined via principal components and variances, respectively.

Let geophysical data set be observed with n trials. If the number of observational locations is p , we have p -dimensional data space, and ones can build an $n \times p$ data matrix \mathbf{D} . Each row represents a p -dimensional position vector in the coordinate system where each axis measures ob-

servations at the corresponding stations. The distribution of the position vectors can be fitted by p -dimensional ellipsoid in this space. The shape of the ellipsoid provides an intuitive figure about the principal components of \mathbf{D} and corresponding variances. The axial vectors of the ellipsoid that orthogonal to each other are equivalent to principal components of \mathbf{D} . Each corresponding variance is simply a squared sum of projected length of p -position vectors on the corresponding axis. If \mathbf{D} can be fitted to an ellipsoid that has the largest variance along a major axis, then major portion of the observations can be represented by the axis. The other axis that has the 2nd largest variance can also be found while it is orthogonal to the major axis of the largest variance. Subsequently, other axes with lesser variances can be determined. This indicates that important parts of data set can be explained by several largest axes of the fitted ellipsoid, and thus we can interpret observational data in lesser dimensional space than p .

The eigendecomposition can be useful to find the axis that could explain geophysical data better than other axes in the space. The axis is determined in a way that the variance along the axis has the largest value. To obtain the direction of the axis, ones first assume that $\hat{\mathbf{v}}$ is a unit column vector parallel to the axis. The data matrix \mathbf{D} can be projected into $\hat{\mathbf{v}}$, and the resulting column vector \mathbf{u} is

$$\mathbf{u} = \mathbf{D}\hat{\mathbf{v}}, \quad \mathbf{u} = (u_1, u_2, \dots, u_i, \dots, u_n)^T. \quad (2.31)$$

The vector \mathbf{u} represents projections of n data points onto $\hat{\mathbf{v}}$, and its

variance is as follow:

$$\text{var}(\mathbf{u}) = u_1^2 + u_2^2 + \cdots + u_n^2 = \mathbf{u}^T \mathbf{u}. \quad (2.32)$$

Note that $\hat{\mathbf{v}}$ is a unit vector and number of its elements is p , equivalent to the dimension of the space, while \mathbf{u} (in general not a unit vector) has n elements relating with the observation sets. Since $\hat{\mathbf{v}}$ has been assumed to produce maximum variance, it can be found by satisfying following equation.

$$\hat{\mathbf{v}} = \arg \max\{\text{var}(\mathbf{u})\} = \arg \max\{\hat{\mathbf{v}}^T \mathbf{D}^T \mathbf{D} \hat{\mathbf{v}}\}. \quad (2.33)$$

The Lagrange multiplier method is a typical approach finding extrema of a multivariate function subjected to one or more constraint conditions. In equation (2.33), the constraint condition is given by $\hat{\mathbf{v}}^T \hat{\mathbf{v}} - 1 = 0$. This leads

$$\mathcal{L} = \hat{\mathbf{v}}^T \mathbf{D}^T \mathbf{D} \hat{\mathbf{v}} - \lambda(\hat{\mathbf{v}}^T \hat{\mathbf{v}} - 1), \quad (2.34)$$

where λ is the Lagrange multiplier. Differentiation of equation (2.34) with respect to $\hat{\mathbf{v}}$ gives

$$\begin{aligned} \nabla_{\hat{\mathbf{v}}} \mathcal{L} &= 2\mathbf{D}^T \mathbf{D} \hat{\mathbf{v}} - 2\lambda \hat{\mathbf{v}} = 0 \\ \mathbf{D}^T \mathbf{D} \hat{\mathbf{v}} &= \lambda \hat{\mathbf{v}}. \end{aligned} \quad (2.35)$$

Thus, λ is an eigenvalue of $\mathbf{D}^T \mathbf{D}$ and $\hat{\mathbf{v}}$ is the corresponding eigenvector. Since $\mathbf{D}^T \mathbf{D}$ is a symmetric matrix, ones can find one or more vectors satisfying equation (2.35). Among them, some $\hat{\mathbf{v}}$ vectors can be selected to effectively represent the data matrix \mathbf{D} . The criterion is to choose $\hat{\mathbf{v}}$ vectors that have larger variances that are equivalently eigenvalues of

corresponding vectors. This can be easily proved by pre-multiplying equation (2.35) by the transpose of $\hat{\mathbf{v}}$, which yield,

$$\begin{aligned}\hat{\mathbf{v}}^T \mathbf{D}^T \mathbf{D} \hat{\mathbf{v}} &= \hat{\mathbf{v}}^T \lambda \hat{\mathbf{v}} \\ (\mathbf{D} \hat{\mathbf{v}})^T \mathbf{D} \hat{\mathbf{v}} &= \lambda \hat{\mathbf{v}}^T \hat{\mathbf{v}} \\ \mathbf{u}^T \mathbf{u} &= \lambda.\end{aligned}\tag{2.36}$$

Consequently, the eigenvector of $\mathbf{D}^T \mathbf{D}$ with the largest eigenvalue is parallel to an axis along which the maximum portion of observation data \mathbf{D} is explained. The second and following axes that explain as large portion of the data as possible can also be found in equation (2.35) accordingly to their corresponding eigenvalues. Since eigenvectors for symmetric matrix are always orthogonal to each other, a projected data space into subset of eigenvectors based on eigenvalue criterion is a new data space with lesser dimension than p .

2.2.2 Singular Value Decomposition

Let \mathbf{X} be an $n \times p$ data matrix, and \mathbf{X} can be decomposed via SVD into three matrix as follow:

$$\mathbf{X} = \mathbf{U} \mathbf{\Sigma} \mathbf{V}^T,\tag{2.37}$$

where \mathbf{U} is an $n \times n$ square unitary matrix and, its columns are called as left singular vector. \mathbf{V} is also a square unitary matrix of order p whose columns are called as right singular vector. $\mathbf{\Sigma}$ is an $n \times p$ rectangular diagonal matrix with the singular values of \mathbf{X} on the main diagonal. Since SVD is closely related with eigendecomposition, it is convenient to derive the SVD procedure using eigendecomposition.

Equation (2.35) is for one of eigenvectors and corresponding eigenvalue for $\mathbf{D}^T \mathbf{D}$ matrix. Let \mathbf{V} be an orthogonal matrix comprising all eigenvectors of $\mathbf{D}^T \mathbf{D}$, $[\hat{\mathbf{v}}_1 \hat{\mathbf{v}}_2 \cdots \hat{\mathbf{v}}_p]$, at its columns, and $\mathbf{\Lambda}$ be a diagonal matrix of corresponding eigenvalues, i.e., $\mathbf{\Lambda} = \text{diag}(\lambda_1, \lambda_2, \cdots, \lambda_p)$. Then the equation (2.35) can be generalized for eigenvalues and corresponding eigenvectors as in equation (2.38),

$$\mathbf{D}^T \mathbf{D} \mathbf{V} = \mathbf{V} \mathbf{\Lambda}. \quad (2.38)$$

Since \mathbf{u} in equation (2.31) are, in general, non-unit vectors, they are normalized by its length according to equation (2.36), i.e., $\mathbf{u} = \sigma \hat{\mathbf{u}}$, where $\sigma = +\sqrt{\lambda}$. This normalization converts equation (2.31) into the matrix form,

$$\mathbf{U} \mathbf{\Sigma} = \mathbf{D} \mathbf{V}, \quad (2.39)$$

where $\mathbf{\Sigma} = \text{diag}(\sigma_1, \sigma_2, \cdots, \sigma_p)$, and hence $\mathbf{\Lambda} = \mathbf{\Sigma}^2$. $\mathbf{U} = [\hat{\mathbf{u}}_1 \hat{\mathbf{u}}_2 \cdots \hat{\mathbf{u}}_p]$ has normal vectors of \mathbf{u} as its columns. If the equation (2.35) is multiplied by \mathbf{D} , it is given by

$$\begin{aligned} \mathbf{D} \mathbf{D}^T \mathbf{D} \hat{\mathbf{v}} &= \mathbf{D} \lambda \hat{\mathbf{v}} \\ \mathbf{D} \mathbf{D}^T (\mathbf{D} \hat{\mathbf{v}}) &= \lambda (\mathbf{D} \hat{\mathbf{v}}) \\ \mathbf{D} \mathbf{D}^T \mathbf{u} &= \lambda \mathbf{u}. \end{aligned} \quad (2.40)$$

The last line of equation (2.40) gives another eigenvalue problem for the symmetry matrix, $\mathbf{D} \mathbf{D}^T$. If \mathbf{u} is non-zero (i.e., $\mathbf{D} \hat{\mathbf{v}} \neq 0$), then \mathbf{u} is an eigenvectors of $\mathbf{D} \mathbf{D}^T$ by definition of eigenvalue, and thus they are all orthogonal each other. Consequently, their normal vectors $\hat{\mathbf{u}}$ are also orthonormal vectors, similar to $\hat{\mathbf{v}}$ in equation (2.35).

Equations (2.35) and (2.40) indicate that non-zero eigenvalues of $\mathbf{D}^T \mathbf{D}$

are identical to those of $\mathbf{D}\mathbf{D}^T$. On the other hand, λ in equation (2.35) that equals to zero, if exists, immediately gives $\mathbf{D}\hat{\mathbf{v}} = 0$ and so this λ and corresponding $\hat{\mathbf{v}}$ are excluded from equation (2.40) by definition of eigenvector. This selection procedure for eigenvalues of $\mathbf{D}^T\mathbf{D}$ is also applied to verify eigenvalues of $\mathbf{D}\mathbf{D}^T$. Therefore, only common eigenvalues of $\mathbf{D}^T\mathbf{D}$ and $\mathbf{D}\mathbf{D}^T$, i.e., $\lambda_1 \geq \lambda_2 \geq \dots \geq \lambda_s > 0$, where $s = \min(n, p)$, are chosen in converting into matrix representation. This choice of common eigenvalues establishes the size of $\mathbf{\Sigma}$ and \mathbf{U} to $n \times p$ and $n \times n$, respectively.

With inserting equation (2.39) into equation (2.38), the following matrix representation is obtained by

$$\mathbf{D}^T\mathbf{U}\mathbf{\Sigma} = \mathbf{V}\mathbf{\Lambda}. \quad (2.41)$$

Multiplying equation (2.41) by $\mathbf{\Sigma}$ and exploiting relationship of $\mathbf{\Lambda} = \mathbf{\Sigma}^2$ gives

$$\begin{aligned} \mathbf{D}^T\mathbf{U}\mathbf{\Sigma}^2 &= \mathbf{V}\mathbf{\Lambda}\mathbf{\Sigma} \\ \mathbf{D}^T\mathbf{U} &= \mathbf{V}\mathbf{\Sigma}. \end{aligned} \quad (2.42)$$

Multiplying equation (2.42) by transpose of orthogonal matrix, \mathbf{U} , provide the following relationship.

$$\begin{aligned} \mathbf{D}^T\mathbf{U}\mathbf{U}^T &= \mathbf{V}\mathbf{\Sigma}\mathbf{U}^T \\ \mathbf{D} &= \mathbf{U}\mathbf{\Sigma}\mathbf{V}^T. \end{aligned} \quad (2.43)$$

The result of equation (2.43) is identical with equation (2.37).

Chapter 3. Amazon River

discharge estimates

3.1 Introduction

Continuous monitoring of river discharge is essential to understand the hydrological cycle and to manage water resources and hydrological disasters [IPCC, 2014; Herschy, 2009]. Its variation with inter-annual and longer time scales is also an integrated measure of global and regional climate and hydrological changes [Knutti *et al.*, 2004; Milly *et al.*, 2002; Nohara *et al.*, 2006; Richey *et al.*, 1989; Shabalova *et al.*, 2003]. Discharge is usually measured across the stream at gauge stations with Acoustic Doppler Current Profiler (ADCP), which uses sound waves to calculate current velocity profiles and its water depth [Kostaschuk *et al.*, 2004; Simpson and Oltmann, 1993]. However, limitations of the ADCP, such as high cost and difficulty of field experiment, often make frequent and automated discharge measurements infeasible particularly for large rivers those with complex flow paths. To acquire continuous time series of river discharge at in-situ stations, the regression analysis of an empirical relationship between discharge and water level data has been adopted as an alternative because the latter can be automatically observable. The water level versus discharge plot constructed to estimate discharge from water level is called the rating curve. Based on the empirical relationship represented by the rating curve, river discharge can be indirectly ‘estimated’

from water level observations.

However, the empirical relationship naturally varies over time due to the geomorphological changes of river base by erosion and deposition [*Jalbert et al.*, 2011]. In addition, intermittent development of new floodplain and formation of episodic braided channels in flood season further increase the uncertainty of the rating curve analysis [*Alsdorf and Lettenmaier*, 2003; *Di Baldassarre and Montanari*, 2009; *Di Baldassarre and Claps*, 2010; *Leonard et al.*, 2000]. This is particularly true for the Amazon River because significant amount of water can flow outside the poorly defined main river channel during flooding. Therefore, it is difficult to estimate discharge during extreme floods, such as the recent one occurred in austral summer of 2009 [*Filizola et al.*, 2014]. Furthermore, there would be additional uncertainty in the empirical relationship for such high record events because the ‘extreme’ events inherently represent a small subset of the water level vs. discharge samples and whose measurements are often limited for safety reasons [*Lang et al.*, 2010; *Petersen-Overleir and Reitan*, 2009].

As an alternative approach, satellite remote sensing has been applied for estimating river discharge [*Alsdorf and Lettenmaier*, 2003]. For rivers with well-established rating curve, remote observations of water surface height can yield estimations of discharge from the empirical relationship. *Kouraev et al.* [2004] and *Zakharova et al.* [2006] used water heights derived from satellite altimetry to determine discharge in the Ob and Amazon Basins, respectively. Satellite imagery methods based on optical, infrared and microwave radar imagery (e.g., MODIS, Landsat and

ERS) are able to determine horizontal water extent, which is the boundaries between water and land, and in turn can produce water height by combination with high-resolution digital elevation model [Smith, 1997; Xu *et al.*, 2004]. The imagery method is useful for rivers in which discharge changes are insensitive to water height variation, such as braided or temporary flooded channels. In this case, extent-discharge rating curve is necessary to estimate discharge from water extent [Smith, 1997]. All of those methods explained above share similar empirical relationship between water surface geometry (height or extent) and discharge [Leon *et al.*, 2006]. Therefore, those satellite-based discharge estimation is also suffered from the similar limitation to the in-situ observation [Alsdorf *et al.*, 2007; Bjerklie *et al.*, 2003].

River discharge estimate based on satellite gravity observations poses an alternative method that does not require *a priori* empirical relation because it uses the gravity changes induced by water mass variations in contrast with the altimetry or optical imagery based approaches. Syed *et al.* [2005] estimated the Amazon and Mississippi River discharge based on water storage variations observed by GRACE time-varying gravity data and precipitation and evaporation computed from European Centre for Medium-Range Forecasts (ECMWF) operational forecast analyses. They combined them in a water balance equation (WBE) for river discharge (R_t) estimate:

$$R_t = P_t - E_t - \frac{\partial S_t}{\partial t}, \quad (3.1)$$

where P_t and E_t are accumulation of precipitation and evapotranspiration, respectively, and ∂S_t is water storage variations over the whole basin

at a given month (t). However, this method is susceptible to the errors in precipitation and evapotranspiration from meteorological model, which typically involves fairly large uncertainties, and time-derivative term of water storage in WBE cause larger random noise [Sheffield *et al.*, 2009]. Consequently, there were large discrepancies between in-situ data and estimated river discharge data [Syed *et al.*, 2005].

In this chapter, a new method is presented to estimate the Amazon River discharge based on the GRACE gravity observation. Water storage changes along the main stem of river are extracted using the Empirical Orthogonal Function (EOF) technique. The EOF method is effective in separating error and signal of the GRACE data [Wouters and Schrama, 2007] due to its capacity of finding spatial correlation in spatio-temporal data [Navarra and Simoncini, 2010]. The water mass signal along the main stem recovered from the EOF analysis may include not only water storage variation in the main stem, which is associated with river discharge, but also various water balance components near the main stem, such as surface runoff, soil moisture and groundwater. However, in a fully-humid, tropical region like the Amazon Basin, the relationship between discharge and water storage is a nearly time-invariant system [Riegger and Tourian, 2014]. In addition, the phase difference between river discharge and other water balance components is shorter than a month near the main stem [Alsdorf *et al.*, 2010]. As a result, water storage variations on the main stem recovered from GRACE data decomposed by EOF can be assumed to represent the same temporal variability of the river discharge. In this chapter, water mass variations on the main stem of the Amazon

River is estimated and compared with in-situ discharge data.

3.2 Data and Method

3.2.1 In-situ data for river discharge

The Óbidos station is operated by the ORE-HYBAM project (www.ore-hybam.org). In-situ data from the station is available since 1968. The Óbidos station is the nearest gauge station on the main stem to the mouth of the basin, even though, it is located approximately 800 km upstream from the outlet. The basin area above the Óbidos station is estimated to comprise 80 % of the whole Amazon Basin, and about 90 % of precipitation is captured in this region [Zeng *et al.*, 2008]. The Tapjos and Xingu Rivers, which are confluents with main stem below the Óbidos, contribute only 10 % of water to total mean discharge. Therefore, many hydrologic studies on the Amazon basin have used hydrometric data observed at this station [e.g., Espinoza *et al.*, 2009; Frappart *et al.*, 2013; Marengo, 2005; Marengo *et al.*, 2012; Yoon and Zeng, 2010].

3.2.2 GRACE monthly gravity solutions

To investigate water mass change, monthly GRACE solutions, determined by the Center for Space Research (CSR), University of Texas at Austin, are used in this study. The latest release (RL05) of GRACE Level-2 data consists of fully normalized spherical harmonics (SH) gravity coefficients up to degree and order 60 [Bettadpur, 2012]. In this chapter, 124 monthly datasets from January 2003 to December 2013 is used, and interpolated the missing months (Jun 2003; Jan and Jun, 2011; May and Oct, 2012; Mar, Aug and Sep, 2013) in SH domain, yielding 132 monthly time-series for 11-years. Due to the unreliability of the degree-2 zonal

harmonic (C20) coefficients, they are replaced with results from Satellite Laser Ranging (SLR) observation [*Cheng and Tapley, 2004*]. Post-glacial rebound (PGR) effects are corrected by the ICE-5G PGR model [*A et al., 2013*]. Peculiar north-south patterns in GRACE gravity solutions are parameterized by a polynomial fitting and removed from GRACE gravity solutions [*Swenson and Wahr, 2006*]. Finally surface mass change at latitude and longitude grid with 0.5° interval in terms of equivalent water thickness (EWT) [*Wahr et al., 1998*] is computed from the reduced SH. Since gravity variations associated with tides, atmospheric pressure and ocean bottom pressure are corrected during determination of GRACE gravity solutions, the derived EWT over Amazon nominally includes surface water in river, lake and floodplain and subsurface water in soil and aquifer.

3.2.3 Rotated EOF method

The EWT fields from the reduced GRACE SH data are still contaminated by residual noise, and it is commonly removed by Gaussian smoothing [*Klees et al., 2008; Schmidt et al., 2008; Tamisiea et al., 2007*]. However, spatial averaging filters cause some signal loss, termed leakage error [*Longuevergne et al., 2010; Swenson and Wahr, 2002*]. Moreover, after the spatial filtering, the spatial resolution of the EWT field decreases, and this makes it difficult to identify water mass signal of main stem. The EOF analysis is an alternative method for GRACE data to separate signals from noise without diminishing spatial resolution [*Wouters and Schrama, 2007*].

The time-varying EWT fields over Amazon can be rearranged into a single matrix \mathbf{D} with size $n \times p$, in which n and p are numbers of temporal samplings and grids, respectively. In EOF analysis, the \mathbf{D} matrix is decomposed into separate modes that are orthogonal to each other using the singular value decomposition (SVD) [Jolliffe, 2002]:

$$\mathbf{D} = \mathbf{U}\mathbf{S}\mathbf{V}^T, \quad (3.2)$$

where \mathbf{V} and \mathbf{U} are orthogonal matrices with size $n \times n$ and $p \times p$ respectively. The i th column vector of \mathbf{V} represents the i th mode spatial pattern of the dataset and is usually denoted by EOF_i . Similarly, the i th column vector \mathbf{U} (PC_i) shows temporal variations of the i th mode spatial pattern. \mathbf{S} is a rectangular diagonal matrix with size of $n \times p$, and their elements on the main diagonal are singular values of the \mathbf{D} matrix. The singular value of the i th mode (σ_i) represents explained variance for the corresponding mode. The variance fraction of the i th mode is calculated as follow:

$$EV_i = \sigma_i^2 / \sum_{k=1}^N \sigma_k^2 \times 100 \%, \quad N = \min(n, p). \quad (3.3)$$

Frappart *et al.* [2013] attempted to explain each individual mode as a corresponding hydraulic parameter, such as surface runoff, groundwater flow and water storage of floodplain. However interpretation of each mode should be made with caution since hydraulic components are subject to be correlated with each other in a given basin [Alsdorf *et al.*, 2010], and thus a particular hydraulic component cannot be accounted for solely by a single EOF. For example, if the first spatial pattern (EOF_1), which represents

the largest variance, shows a monopole structure on a domain, the second-dominant spatial pattern (*EOF2*) tends to have a dipole structure to be orthogonal to the *EOF1*. The spatial patterns of following modes are also determined by the similar manners [*Hannachi et al.*, 2007]. This nature of EOF decomposition is inevitably problematic for river discharge signal that is confined along river channels. Signal along river channel is likely projected into many EOF modes, and thus interpretation of river discharge from a single EOF mode possibly causes additional uncertainty.

This EOF limitation can be fixed by rotating vectors \mathbf{v} in \mathbf{V} matrix to construct new EOF modes,

$$\mathbf{W} = \mathbf{V}_s \mathbf{R}, \quad \text{with} \quad \mathbf{V}_s = [\mathbf{v}_1 \mathbf{v}_2 \cdots \mathbf{v}_s], \quad (3.4)$$

in which \mathbf{R} is the rotation matrix and s is the number of EOF modes that are assumed to be signal, based on the variance fraction \mathbf{S} in equation (3.2). This modified version is called rotated EOF (REOF). Criterion of the rotation is to find a new EOF mode (\mathbf{W}) that has maximum variance fraction in given grid points: this is equivalent to finding minimum numbers of new EOF modes that are sufficient to synthesize the original values of a grid-point values.

For example, the water mass signal along a river channel that was projected into many EOF modes are re-projected to a single mode, and this new EOF mode has the maximum variance associated with the signal from the channel. There are several different cost functions to maximize the variance. In this chapter, the VARIMAX method is used [*Hannachi*

et al., 2007]. The cost function is

$$f(\mathbf{w}_1, \mathbf{w}_2, \dots, \mathbf{w}_s) = \sum_{k=1}^s \left[p \sum_{i=1}^p w_k^i{}^4 - \left(\sum_{i=1}^p w_k^i{}^2 \right)^2 \right],$$

where w_k^i are the i th grid-point value of the k th REOF spatial pattern (*REOFk*). Rotation angles are iteratively adjusted until the cost function is converged.

3.2.4 Synthetic GRACE data

To verify REOF application for Amazon River discharge estimate from GRACE observation, it is necessary to test the method with synthetic GRACE data. GRACE gravity solutions over land include terrestrial water storage (TWS) changes reflecting mass variations of soil moisture, groundwater, snow (and ice), lakes and water flow on river channels and floodplain [Cazenave and Chen, 2010]. To include those TWS variations into synthetic GRACE data, model outputs from Global Land Data Assimilating System (GLDAS) [Rodell *et al.*, 2004] is used. GLDAS incorporates data assimilations of four different model outputs. In this study, the simulation of TWS changes based on the Common Land Model (CLM) land surface model [Bonan, 1998] is used.

The changes of total TWS for the Amazon basin can be partitioned into soil moisture and surface water storage components [Han *et al.*, 2010]. The soil moisture is simply given by the monthly GLDAS/CLM outputs at each 1-degree grid cell. The surface water storage represents mass variations associated with horizontal water transport through rivers and floodplains, but this component is not modeled in the GLDAS because the

system is mainly focused on the vertical water fluxes. To simulate river discharge, a runoff routing method based on a continuity equation [Okki *et al.*, 1999] is used. This routing method uses linear relationship between surface water storage and runoff, and thus runoff at river channel (i.e., river discharge) can be easily simulated by scaling of corresponding surface water storage. Han *et al.* [2010] solved the continuity equation for runoff routing in a spectral domain within seasonal frequency band to examine annual variations of surface water storage over the Amazon basin. In this study, the surface water storage is simulated by the spectral routing method [Han *et al.*, 2010], but complete set of spectra less than Nyquist frequency is used to construct broadband runoff time series at each grid cell. 3-hourly surface and subsurface runoff data from the GLDAS/CLM are incorporated as input parameters for the continuity equation, and simulated runoff time series at each grid cell is added to the soil moisture variations from the GLDAS/CLM for the total TWS over the basin.

Since real GRACE data is contaminated by errors, it is necessary to combine TWS and GRACE errors for synthetic GRACE data. Errors in the monthly GRACE solutions are mainly attributed to measurement noise and aliasing error from unmodeled atmospheric and oceanic effects [Wahr *et al.*, 2006]. Those errors can be suppressed significantly by a spatial averaging because they are dominant over shorter wavelength [Han *et al.*, 2005; Seo and Wilson, 2005; Wahr *et al.*, 2006]. Therefore, differences between the real GRACE and its smoothed gravity solution may represent GRACE error fields [Seo *et al.*, 2015a; Velicogna and Wahr,

2013]. However, difference between smoothed and unsmoothed GRACE data possibly includes true gravity variations since smoothing can also diminish signals. Therefore, residual mass variations from the difference over the Amazon basin are highly correlated with the simulated TWS changes, and thus the correlated component are removed from the differences for the GRACE error estimate. Finally, TWS changes from soil moisture and runoff and the estimated GRACE errors are combined for the synthetic GRACE data.

Figure 3.1 shows degree amplitudes for the real (black) and synthetic (green) GRACE data over the Amazon basin during the study period from 2003 to 2013. Degree amplitudes for TWS and estimated error are also exhibited in blue and red lines, respectively. The green line (degree amplitude of synthetic GRACE data) shows two peaks around degrees 8 and 57. Peaks at lower and higher degrees are associated with TWS signal (blue) and GRACE error (red), respectively. In addition, the black line is close to the green line, and it indicates that synthetic GRACE data reasonably depicts real GRACE data over the study area.

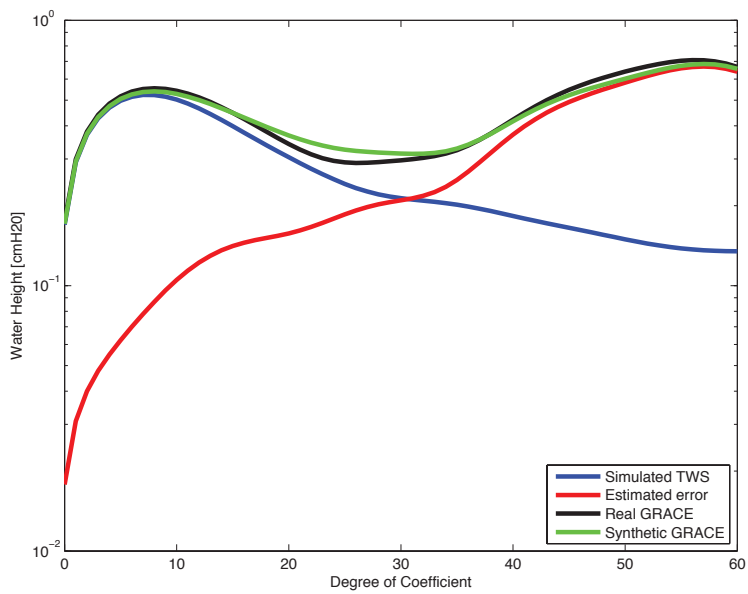


Figure 3.1 Degree amplitudes for real (black) and synthetic (green) GRACE data. The synthetic GRACE data is sum of the simulated TWS (blue) and estimated error (red). The degree amplitude for the real GRACE data agrees well with the synthetic GRACE data.

3.3 Results

3.3.1 Recovering river discharge from the synthetic data

Gridded synthetic GRACE data after de-correlation filtering are decomposed into EOF modes over upstream of the Óbidos station in the Amazon Basin using equation (3.2). Figure 3.2a and b exhibit the spatial patterns of the first two modes ($EOF1-2$), and solid red and dashed blue lines in Figure 3.2c show their corresponding time series ($PC1-2$). In Figure 3.2a and b, the Amazon Basin is bounded in the thick black line, and a main channel and major tributaries are mapped by thin black lines. The grey line marks the eastern boundary of the Óbidos sub-basin whose discharge has been continuously gauged at the Óbidos station (cyan triangle). The “ExVar” above each panel denotes the EV of the corresponding EOF mode in equation (3.3). The first two modes account for 72.8 % of the total variance, which implies that the simulated TWS changes in the basin can be largely represented by the first two modes. The black line in Figure 3.2c shows synthetic river discharge variations at the Óbidos station. All time series in Figure 3.2c are normalized by its standard deviation.

The 1st mode shows the largest apparent anomaly along the main stem (Figure 3.2a, $EOF1$). Its variance fraction, 58.9%, suggests that more than half of the simulated TWS change is associated with TWS along the main stem with the peaks at May and October (red line in Figure 3.2c). However the relatively large amplitudes of the basin-wide $EOF1$ anomaly indicates that the 1st mode include signals associated with not only river discharge on the main stem but also soil moisture variations distributed

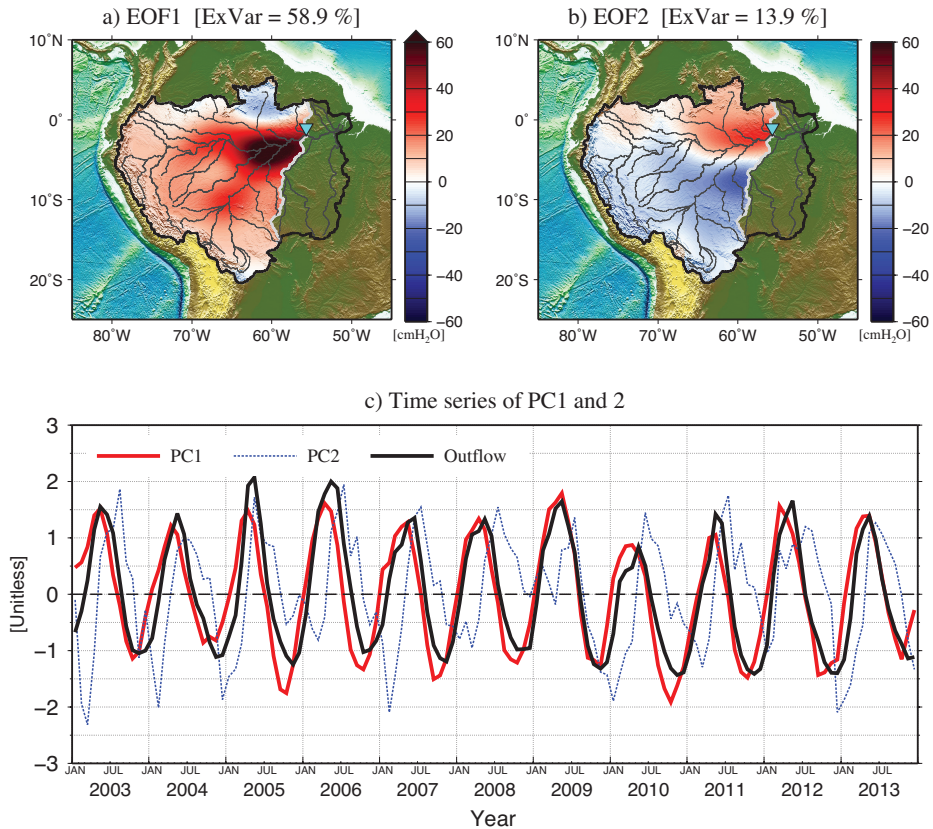


Figure 3.2 EOF results for the synthetic GRACE data over the Óbidos sub-basin. a) The first spatial pattern (*EOF1*) has an apparent anomaly on the main stem. b) The *EOF2* shows a north-south dipole pattern; the northern pole is located on the main stem. c) shows temporal variations of the first mode (*PC1*, red line) and second mode (*PC2*, dash), and synthetic river discharge at Óbidos station (black line).

on the whole basin. This combination of two different TWS components in the 1st EOF mode can be also inferred from $PC1$ (red line in Figure 3.2c). Variations of $PC1$ are comparable to those of river discharge at the Óbidos station, but their phases differ about one or two months. This discrepancy is likely because a portion of the main stem signal is projected into the 2nd mode. The spatial pattern of the 2nd mode shows a north-south dipole pattern, and the northern pole is located on the main stem (Figure 3.2b). As a result, river discharge signal on the main stem is likely partitioned into the 1st and 2nd EOF modes.

Because this study aims to extract signal of water mass change from a main stem, additional procedure is required to retrieve the main stem signal from the leading two EOF modes. As an alternative, the VARIMAX method described in Section 3.2.3 is applied to obtain a signal over the main stem area. TWS variations over the Amazon Basin are recovered using the 1st and 2nd modes, and they are transformed into another coordinate system based on basis rotation. The resulting rotated EOF modes are shown in Figure 3.3. $REOF1$ spatial pattern (Figure 3.3a) shows a very similar structure to that of the first EOF ($EOF1$, Figure 3.2a) while a positive anomaly is more closely confined only along the main stem. The variance fraction of the 1st mode is 42.7%, which is smaller than that of the 1st mode of EOF. This is because the TWS pattern from the 1st rotated EOF mode is confined on the main stem while that of the 1st EOF mode widely spreads over whole basin. The 2nd mode here shows a similar dipole pattern to the 2nd EOF mode shown in Figure 3.2b. However, the 2nd mode from the rotated EOF does not show any apparent

anomaly close to the Óbidos station but the large anomaly is located in the southern part of the basin (Figure 3.3b). This indicates that most of the signal of water storage variation on the main stem can be depicted by the 1st rotated EOF mode.

The effective separation of water storage signal of main stem is also found in the temporal variation of 1st and 2nd modes of the rotated EOF. Solid red and dashed blue lines in Figure 3.3c show the temporal rotated EOF mode 1 and 2 (*RPC1* and *RPC2*), and solid black line is identical to that of in Figure 3.2c. They are normalized similar to Figures 3.2c. *RPC1* agrees remarkably well with synthetic river discharge at the Óbidos station except for negative peaks. The slight discrepancies during low water season are likely due to the effect of base flow, not simulated in the routing model. To simulate more realistic surface water storage including base flow, different residence time parameters for subsurface runoff slower than those of surface runoff are required in solving routing model [Liston *et al.*, 1994], but the routing model in this study deals with the integrated surface and subsurface runoff for simplicity. Temporal variations of *RPC2* precede those of *RPC1* about two or three months. As shown in Figure 3.3b, the *REOF2* shows a large anomaly in the southern basin. This dipole spatial pattern and its phase difference compared to water storage signal along the main stem (i.e., discharge) are caused by soil moisture variations between the Southern and Northern basin from GLDAS/CLM and is a typical spatio-temporal variations of water storage in the Amazon Basin [Marengo, 2005]. As a result, the rotated EOF effectively separates main stem signals from the synthetic data, and thus *RPC1* can be useful

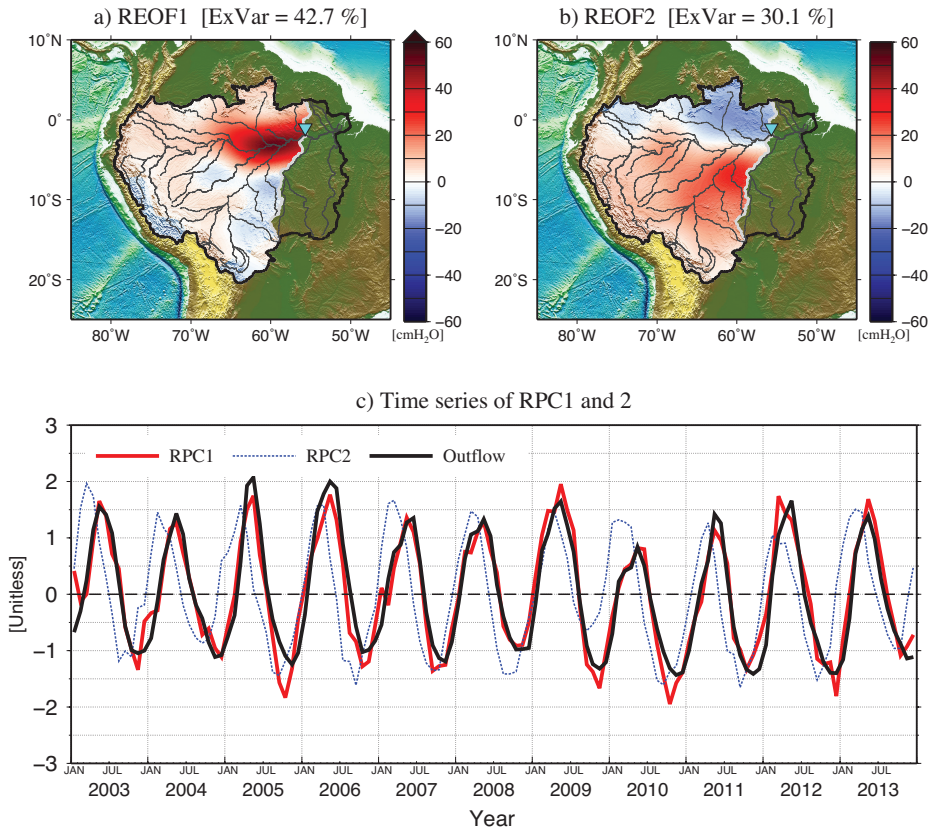


Figure 3.3 REOF results for the synthetic GRACE data over the Óbidos sub-basin. These are reconstructed from the first two modes in the EOF by rotating basis. a) *REOF1* anomaly is evidently confined in the main stem. b) *REOF2* shows its spatial pattern is outside the main stem. c) shows the temporal variations of the first mode (*RPC1*, red line) and second mode (*RPC2*, dash). The black line is identical to c) in Figure 3.2.

to recover river discharge of the basin.

The REOF method can be used to estimate river discharge for the entire Amazon Basin. This is the exactly the same procedure described above except using the Amazon basin (represented by thick solid line in Figure 3.2) instead of Óbidos basin. The examination is particularly important because in-situ discharge observation at the outermost river mouth has been extremely difficult due to the interference of seawater intrusion [Kosuth *et al.*, 2000]. Red line of Figure 3.4 shows temporal variations of the 1st rotated EOF on the synthetic GRACE data (*RPC1*) for the entire Amazon basin. Black line exhibits simulated river discharge variations at the basin mouth. Similar to the synthetic test for the Óbidos basin, two time series agree remarkably well with each other during the course of the study period. This result implies that total river discharge of the Amazon Basin, which has not been gauged by an in-situ station, can be determined by the GRACE gravity solutions.

3.3.2 Recovering river discharge from the real GRACE solutions

As examined with synthetic GRACE data, the REOF method is useful to recover river discharge variations. In this section, Amazon River discharge is estimated from the real GRACE data with the REOF method and compared with in-situ discharge data at the Óbidos station. Using equation (3.2), the gridded real GRACE data over the Óbidos Basin is decomposed into EOF modes. Figure 3.5 shows the spatial patterns of the first two modes (*EOF1-2*) and their corresponding time series (*PC1-2*).

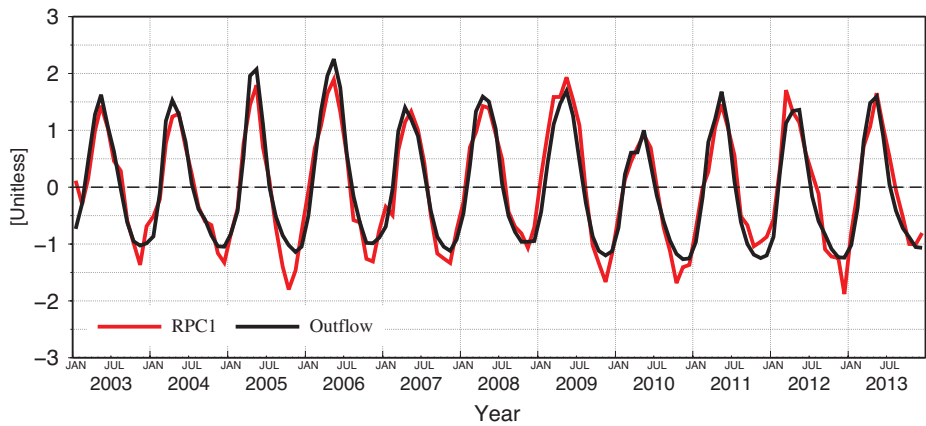


Figure 3.4 REOF time series for the synthetic GRACE data at the basin mouth of Amazon. The red line shows temporal variations of the first REOF mode. The black line is synthetic river discharge computed by routing model at outmost river mouth of Amazon Basin. Two time series agrees well each other through study time period.

The first two modes account for 88.9% of the total variance, about 16% higher than the synthetic data. This implies that the real GRACE data may have higher signal to noise ratio than the synthetic GRACE data. The *EOF1* and 2 (Figure 3.5a and b, respectively) show very similar spatial patterns to those from synthetic GRACE data (Figure 3.2): *EOF1* exhibits large TWS pattern along the main stem while non-negligible anomaly is apparent over the entire basin, and *EOF2* shows a clear north-south dipole pattern. Their corresponding time series (*PC1* and 2 in Figure 3.5c) are also very similar to the case of synthetic GRACE data. Variations of *PC1* (solid red line) are close to those of in-situ river discharge at the Óbidos station while there exists one or two months phase difference.

Similar to the synthetic GRACE data, the VARIMAX algorithm is used to rotate the leading two modes from the conventional EOF. Figure 3.6 shows the resulting rotated EOF modes and it also exhibits similar spatial patterns (*REOF1* and 2 in Figure 3.6a and b, respectively) and corresponding time series (*RPC1* and 2 in Figure 3.6c) to those of the synthetic data (Figure 3.3). *RPC1* (red) shows a similar phase to the in-situ discharge data (black). In particular, negative peaks of both time series agree well each other unlike the case of synthetic test. The positive peaks of *RPC1* show apparent discrepancies than those of in-situ data. The most significant difference is found at the 2009 flood, which was the *once-in-a-century* event in this basin [Marengo *et al.*, 2012]: *RPC1* clearly shows the largest flood while in-situ discharge data at the Óbidos station (black) does not show this extreme record in 2009.

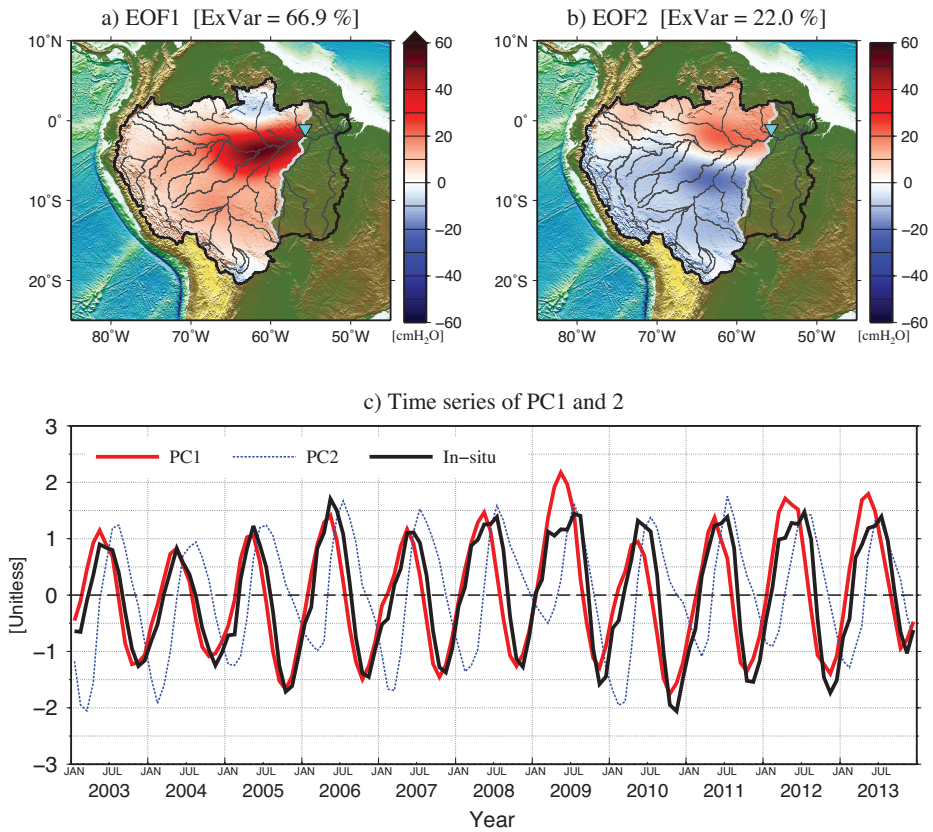


Figure 3.5 Similar figure to Figure 3.2 except for real GRACE and in-situ data. Spatial pattern and temporal variability from real GRACE data after EOF decomposition are very close to those from synthetic GRACE data (shown in Figure 3.2)

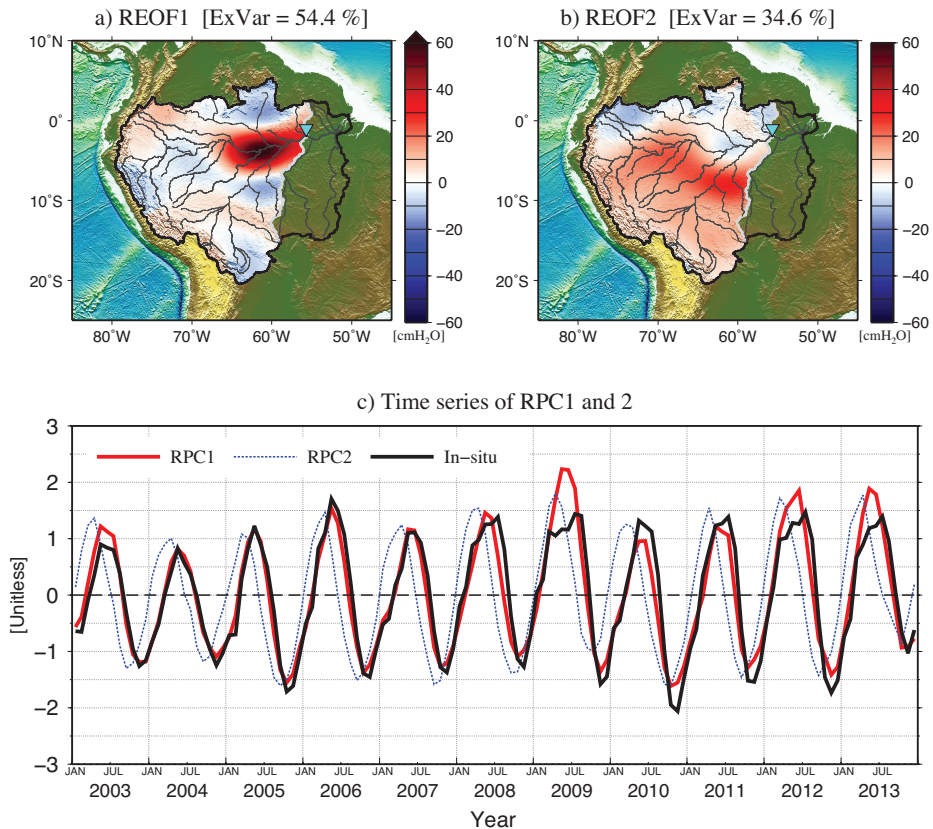


Figure 3.6 Similar figure to Figure 3.3 except for real GRACE and in-situ data. Spatial pattern and temporal variability from real GRACE data after REOF decomposition are very close to those from synthetic GRACE data (shown in Figure 3.3). Red (temporal variations of the 1st REOF mode) and black (in-situ discharge data at Óbidos) lines agree with each other except flooding season

This discrepancy is possibly due to different methods to measure the discharge of Amazon River that complex floodplain is developed during wet seasons. The northern bank of the reach of Amazon River at the Óbidos is well confined, but at the opposite side narrow natural levee separates it from the Curuaí floodplain, one of the largest floodplain in the basin. As water height increases in flood season, some portion of water flow in the Óbidos channel starts to detour the Óbidos station through this floodplain. According to *Oltman* [1968], the bypassing water volume through the Curuaí varies from 0 to 10 % of total discharge depending on the hydraulic conditions, such as surface water slope and bed roughness of the floodplain. Since the in-situ observation is a point measurement in a single river channel, discharge data obtained in the Óbidos station can differ from the water volume that drains out of the basin. In case of the rotated EOF that decomposes GRACE observation, on the other hand, river discharge is determined over the whole basin with focusing into the main stem area and thus represents total water mass flowing out of the basin through its mouth. This indicates that the point-based in-situ measurement may not capture the total flow when new flow paths, such as a new large floodplain, are formed during the peak flooding season [*Als Dorf and Lettenmaier*, 2003].

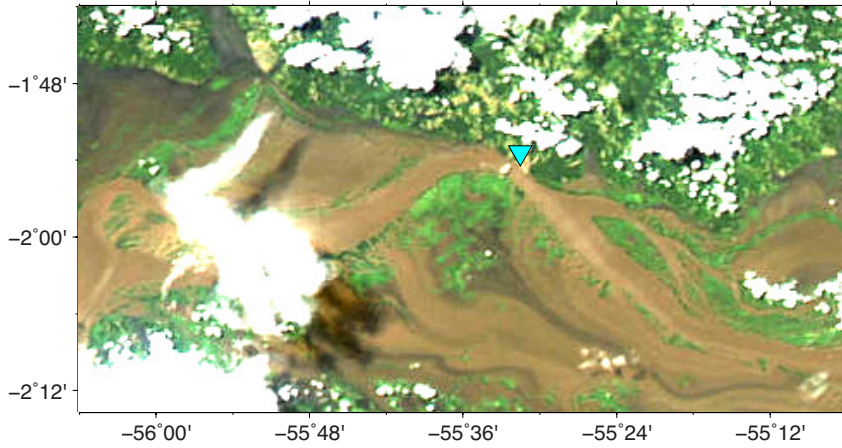
Figure 3.7 compares the MODIS satellite images around the Óbidos station in June 2009 (a) and June 2010 (b), which represent the once-in-a-century (2009) and an ordinary (2010) flooding events, respectively. The location of the Óbidos station is marked by cyan triangle. Figure 3.7a clearly exhibits wide flow paths in the south, which is not seen in the

2010 flood image. This implies that a large portion of total discharge flowed through the southern floodplain in 2009 may be missed in the in-situ discharge measurements at the Óbidos station. On the other hand, Figure 3.7b shows that most of discharge was confined along the main stem. Similar differences between *RPC1* and in-situ data are also shown during flood season in 2012 and 2013, indicating that in-situ observation may underestimate river discharge during flooding.

Since *RPC1* (red line in Figure 3.6c) only shows normalized river discharge, appropriate scaling of *RPC1* is necessary to quantify amount of water volume of discharge in the basin. The WBE-based discharge from equation (3.1) is used to adjust amplitude of the *RPC1*. For precipitation and evaporation, ERA-Interim data are used [Dee *et al.*, 2011], and the water storage variations are computed from GRACE data. To suppress noise included in the GRACE data, reconstructed data from the first two EOF modes is used. The resulting WBE-based discharge (blue) is additionally shown in Figure 3.8. WBE-based discharge has the higher month-to-month variability than those of in-situ data and *RPC1*. The higher variability is likely associated with errors in the reanalysis and GRACE after the first order time-derivative. However, its overall pattern agrees with *RPC1* and the in-situ measurement, and thus the WBE-based estimate is useful to auxiliary information for scaling of *RPC1*.

Figure 3.9a shows *RPC1* and WBE river discharge and the regression between the two. As shown in Figure 3.8, Figure 3.9a exhibits a similar variation between WBE river discharge and *RPC1*. Based on the linear regression, *RPC1*-based river discharge can be estimated by adding a mean

a) 2009.06.16.



b) 2010.06.07.

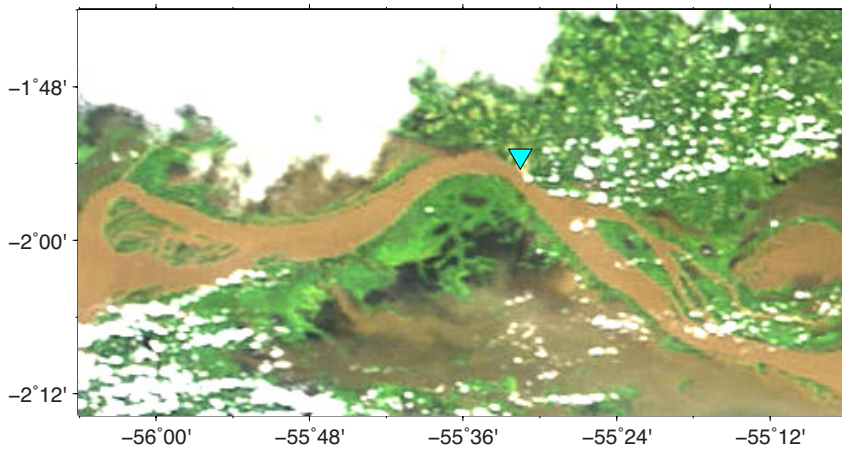


Figure 3.7 MODIS satellite images around the Óbidos station in June 2009 (a) and June 2010 (b). The location of the Óbidos station is marked by cyan triangle. The river flows eastward (to right) in this region. a) clearly exhibits wide flow paths in the south implying a large portion of water volume may be missed in the in-situ discharge measurements at the Óbidos station. b) shows that most of discharge was confined along the main stem.

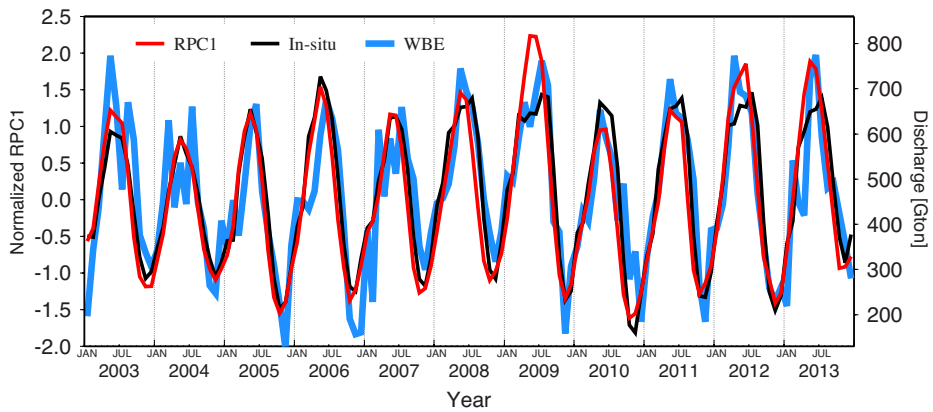


Figure 3.8 Comparisons of $RPC1$ with WBE and In-situ. The red and black lines are identical to those of c) in Figure 3.6. The blue line represents WBE-based discharge computed by equation (3.1). WBE-based discharge has the higher month-to-month variability than those of in-situ data and $RPC1$, but its overall pattern agrees with $RPC1$ and the in-situ measurement. This implies that the WBE-based estimate is useful to auxiliary information for scaling of $RPC1$.

and scaling amplitude. Figure 3.9b exhibits the probability density of the difference between WBE and *RPC1* river discharge. The probability density in Figure 3.9b is associated with misfits between the two that is suspicious of error in WBE river discharge estimate. The histogram appears normally distributed, and thus the higher temporal variations (discrepancy between *RPC1* and WBE-based discharge) are likely noise. Those results imply that the regression analysis between *RPC1* and WBE-based discharge is reasonably adopted for scaling of *RPC1* data. *Rudorff et al.* [2014] estimated that about 2% of the annual discharge detoured around the main channel during 2009 based on an inundation model. The approach based on GRACE data gives that the 2009 annual discharge from *RPC1* is 6,650 *Gt*, while in-situ discharge is 6,250 *Gt*. The difference is about 6% of annual discharge, and sizable portion of it is likely due to the water flow via floodplain. Figure 3.8 shows that discharge discrepancy between in-situ and *RPC1* is apparent since 2008. This is probably because the method for estimating discharge at the station was adjusted to accurately determine water volume passing the channel (Ore-Hybam, personal communication, 2014).

This novel method can be also extended to the entire Amazon Basin. Red line in Figure 3.10 shows the total discharge over the entire Amazon Basin estimated by the combination of rotated EOF and WBE of GRACE time-varying gravity, and black line shows the discharge over Óbidos basin that is identical to black line in Figure 3.8. Figure 3.10 shows that the total discharge over Amazon Basin is about 23% greater than the Óbidos discharge, and during June 2009, it reached 1,050 *Gt*,

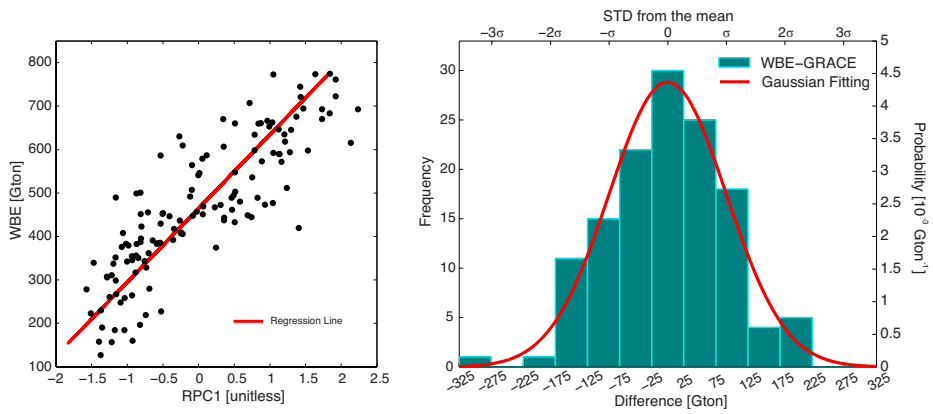


Figure 3.9 Regression results between WBE and *RPC1*. a) *RPC1* exhibits similar variations to WBE-based river discharge. Based on the linear regression, *RPC1*-based river discharge can be estimated by adding a mean and scaling amplitude. b) shows the probability density of the difference between WBE and *RPC1* river discharge. The histogram appears normally distributed, and thus the higher temporal variations (discrepancy between *RPC1* and WBE-based discharge) are likely noise.

which is a unique event exceed 1,000 *Gt* during the study period. Blue line in Figure 3.10 represents sum of in-situ discharge from the Óbidos, Itaituba and Altamira stations. The latter two stations are located at two rivers confluent below Óbidos station. The discharge is much closer to red line than those of the Óbidos basin because it incorporates contribution of rest basin outside the Óbidos basin, but it is still smaller than the red line because the three in-situ stations cannot observe net river discharge of the entire Amazon Basin. Blue line precedes black and red lines about one month because both additional discharge data are gauged from southern basin, and contribution from northeastern basin is missed because in-situ data is not available at the region.

3.4 Discussion

In-situ river discharge has been estimated at a gauge station based on an empirical relation between water level and river discharge observations. This is because water level observation is easier than discharge observation. In the case of extreme high flood, however, the empirical relation is not likely to be accurate since at high values observations may be too scarce to develop reliable relationship between the two. In addition, floodplain is likely inundated, and thus river flow detours around gauge stations. Remote sensing for river discharge estimate has been examined as an alternative method for the in-situ observation, particularly in the context of decreasing numbers of in-situ stations globally [Alsdorf and Lettenmaier, 2003; Shiklomanov *et al.*, 2002]. However, application of remote sensing for river discharge observation has been limited since it still needs in-situ data or meteorological estimate that causes additional uncertainty.

To overcome the limitations of the remote sensing, alternative method is developed for Amazon River discharge. The method use TWS variations from GRACE and extract signals associated with Amazon River discharge variations based on rotated EOF analysis. The leading REOF pattern (*REOF1*) shows the TWS signal is confined along the main stem of the river, and temporal variability (*RPC1*) agrees remarkably well with in-situ data, except during the flood season. The discrepancy during flooding is likely due to the detoured water when the floodplain is inundated, and thus in-situ observation is likely to underestimate it.

One important limitation of rotated EOF decomposition of TWS,

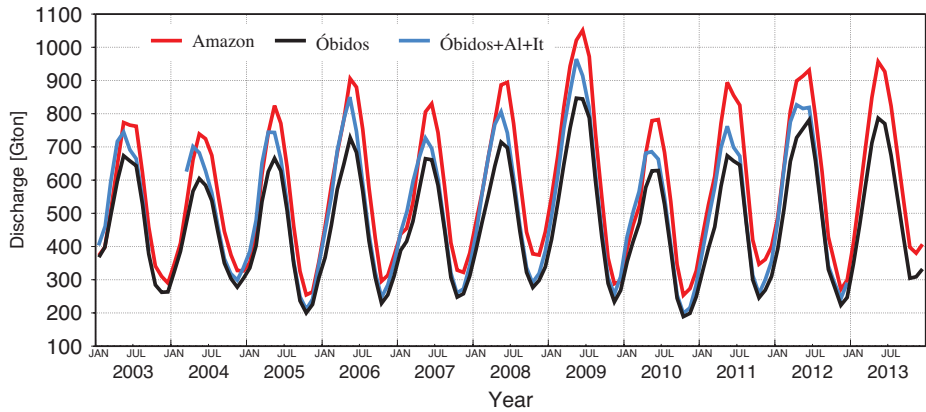


Figure 3.10 Total discharge estimates for the Amazon Basin. Red line shows the total discharge over the entire Amazon Basin estimated by the combination of rotated EOF and WBE of GRACE time-varying gravity. Black line shows the discharge over Óbidos basin. The total discharge over Amazon Basin is about 23% greater than the Óbidos discharge. Blue line represents sum of in-situ discharge from the Óbidos, Itaituba and Altamira stations. The latter two stations are located at two rivers confluent below Óbidos station.

however, is that only relative river discharge variations are estimated: *RPC1* for Amazon Basin shows normalized variations of river discharge. It is suggested that regression between *RPC1* and WBE-based river discharge is useful to estimate physical unit of river discharge from *RPC1*. This method is potentially applicable for discharge estimates at basin mouths over large river basins, which are not observed by in-situ gauge but significant to regional or global climate change.

Chapter 4. De-correlation of GRACE data on the GrIS

4.1 Introduction

During the recent decades, significant efforts have been made for accurate estimation of ice loss in Greenland ice sheet (GrIS), since acceleration of GrIS mass loss has emerged. Due to the sparse in-situ measurements for GrIS, ice loss estimations mostly rely on remote sensing observations. These methods include radar and laser altimeters based on airborne or space-borne for surface elevation change [Zwally *et al.*, 2011] and satellite interferometric synthetic-aperture radar (InSAR) for ice flow of outlet glaciers [Rignot and Mouginot, 2012]. However, there are some limitations in conversion of their observations to ice mass changes because these methods require assumptions of ice thickness and density [Khan *et al.*, 2015]. Since launch of GRACE which is dedicated to observe Earth's gravity change, direct observation of mass loss in GrIS has become possible. Recent GRACE results showed significant ice mass loss in GrIS: ice loss rate and its acceleration range from -249 Gt/yr to -280 Gt/yr and -21 Gt/yr^2 to -31 Gt/yr^2 , respectively [Rignot *et al.*, 2011; Schrama *et al.*, 2014; Velicogna and Wahr, 2013; Wouters *et al.*, 2013]. In addition, Chen *et al.* [2013] estimated that GrIS contribution to GMSL rise is 0.69 mm/yr , which is larger than that from Antarctica (0.50 mm/yr) or mountain glaciers (0.54 mm/yr).

In addition to inter-annual to secular ice mass variations, GrIS mass changes have clear month-to-month fluctuations [Wouters *et al.*, 2008]. These shorter variations are mostly associated with surface mass balance (SMB) including precipitation and meltwater runoff [van den Broeke *et al.*, 2009]. Another main cause of the shorter time scale mass fluctuations in GrIS is solid ice discharge at marine-terminating glacier. This contribution comes from ice velocity increase in summer with respect to winter background speed due to meltwater penetration into glaciers and subsequently alter sub-glacial hydrology system [Moon *et al.*, 2014]. However previous GRACE estimates have mainly focused on ice mass loss with inter-annual and longer time scale [e.g., Chen *et al.*, 2011; Seo *et al.*, 2015b].

Even though GRACE provides global gravity variations in monthly time scale, it is challenge to obtain month-to-month variations accurately due to the error, and this limitation is potentially problematic to appraise accurate seasonal mass variations. Global surface mass anomalies from unfiltered GRACE data are dominated by meridional stripes due to the errors in the high degree (l) and order (m) spherical harmonics (SH) coefficients. Swenson and Wahr [2006] found that theses peculiar patterns are associated with correlated variations of SH coefficients and developed a de-correlation filter to suppress the error. Many GRACE applications for GrIS mass balance studies incorporated the de-correlation filter [e.g., Chen *et al.*, 2013, 2011; Seo *et al.*, 2015b] to suppress possible contamination from the correlation error. Harig and Simons [2012], on the other hand, showed the similar results to the previous GrIS studies

without applying the de-correlation filter for GRACE SH. This result indicates that the contribution of the correlation error is likely diminished for the continental scale mass balance estimate. However, a caution is still necessary to examine regional ice mass variations. Unfiltered correlation error may hinder accurate estimate of small-scale ice mass variations in GrIS. In addition, regional ice mass variations are possibly eliminated during de-correlation filtering. This is particularly problematic in GrIS because dominant signals are located along west and east coast, and they are apparently similar to the longitudinal stripes.

Recently, the empirical orthogonal function (EOF) method has been used in GRACE applications [*Chambers, 2006; Frappart et al., 2013; Schrama et al., 2007; Schrama and Wouters, 2011*]. This technique, also known as Principal Component Analysis, decomposes a space-time data set into spatial patterns and corresponding time series. One of the benefits of using this method is that it is amenable to multi-variable data on any grid, regular or not, even in SH domain. *Wouters and Schrama [2007]* applied this method directly on global GRACE Stokes coefficients to isolate correlation errors and validated that their filter effectively recovers signal without attenuation. In this study, the EOF method is applied to GRACE monthly solutions in a different fashion by considering spatial and temporal correlation simultaneously. This approach can recover month-to-month evolution in mass change in GrIS that was possibly filtered out by the de-correlation procedure or prevailed by correlation error when the de-correlation filter was not applied.

4.2 Data and Method

4.2.1 Monthly GRACE solutions

The GRACE solutions represented by Stokes coefficients of SH up to degree and order 60 are determined by the Center for Space Research (CSR), University of Texas at Austin. These solutions provide geoid height with time interval of one month. In this chapter, 132 monthly datasets from January 2003 to August 2014 are used, and interpolated the missing months (Jun 2003; Jan and Jun, 2011; May and Oct, 2012; Mar, Aug and Sep, 2013) in SH domain, yielding 140 monthly time-series for 11-years. This interpolation is conducted because EOF filtering, which is described in following sub-section, requires data set with regular temporal sampling. The omissions of degree-1 coefficients are added by synthetic values using ocean model output and GRACE data [Swenson *et al.*, 2008]. The degree-2 zonal harmonic (C20) coefficients with relatively low reliability are replaced with observations from Satellite Laser Ranging (SLR) observation [Cheng and Tapley, 2004]. Viscoelastic responses from the post-glacial rebound (PGR) are corrected by the recent ICE-5G ice history model [A *et al.*, 2013]. The mean of this reduced SH coefficients is removed from each monthly solution and surface mass change is finally derived [Wahr *et al.*, 1998]. These mass coefficients mostly represent redistribution of surface water with contamination from aliasing and random noise.

4.2.2 Extended EOF

Extended EOF (EEOF) method used in this study is a modified version of EOF, which was initially developed to identify propagation wave in space-temporal dataset [Weare and Nasstrom, 1982]. While the original EOF method just deals with spatially concurrent correlation, EEOF technique also considers temporally lagged correlation at the same time to capture time evolution [Hannachi et al., 2007]. In Greenland, significant mass loss associated with ongoing global warming is observed while seasonal evolution in time and space is also superimposed on the negative mass loss trend. On the other hand, the correlation errors in GRACE data are randomly distributed in time and appear on the map to be longitudinal patterns. Therefore, they could overlap the coastal regions where ice mass changes arise. In this situation, applying EEOF method on the GRACE data can be a good solution to discern seasonal evolution in mass changes from the correlation error.

The EEOF is fundamentally identical to the conventional EOF because both decompose spatio-temporal data into spatial and temporal modes. The differences between two are organization of data matrix before decomposition and reconstruction after decomposition. To clarify EEOF procedure, ones consider spatio-temporal data that its total numbers of spatial and temporal samplings are p and n , respectively. For GRACE gravity solutions, n is the number of months during the study period and p can be the number of sine and cosine coefficients of SH. Each time-varying SH coefficients can be described as a column vector, $\mathbf{d}_j^{(1,n)} = (d_j^1, d_j^2, \dots, d_j^i, \dots, d_j^n)^T$, where j is the location index from 1

to p that indicates a coefficient with certain degree and order. The superscript means that the elements of the column vector for i th month. In conventional EOF, the coefficients can be arranged in an $n \times p$ data matrix, $\mathbf{D} = [\mathbf{d}_1^{(1,n)} \quad \mathbf{d}_2^{(1,n)} \quad \dots \quad \mathbf{d}_p^{(1,n)}]$. On the other hand, the EEOF method segments a column vector $\mathbf{d}_j^{(1,n)}$ into M numbers column vectors that is successively time-lagged. For example, $\mathbf{d}_1^{(1,n)}$ is transformed into a sub-data matrix \mathbf{D}_1^E :

$$\mathbf{D}_1^E = [\mathbf{d}_1^{(1,n-M+1)} \quad \mathbf{d}_1^{(2,n-M+2)} \quad \dots \quad \mathbf{d}_1^{(M,n)}], \quad (4.1)$$

where M is the *window length* parameter. Therefore, the new data matrix \mathbf{D}^E is given by

$$\mathbf{D}^E = [\mathbf{D}_1^E \quad \mathbf{D}_2^E \quad \dots \quad \mathbf{D}_p^E]. \quad (4.2)$$

Compared with \mathbf{D} , this new data matrix \mathbf{D}^E contains additional temporal variations by incorporating spatial and time variations into a single row of the extended data matrix. M can be determined based on the temporal scale of examination. For example, ones can select M as 12 to investigate temporal variability for annual or shorter variations from GRACE monthly data.

The singular value decomposition (SVD) is a simple way to separate a given dataset into spatial patterns and associated time series as follows:

$$\mathbf{D} = \mathbf{U}\mathbf{\Sigma}\mathbf{V}^T, \quad (4.3)$$

where \mathbf{V} and \mathbf{U} are orthogonal matrices, and each column vector of them represents spatial pattern and associated time variation, respectively. $\mathbf{\Sigma}$ is a rectangular diagonal matrix with the singular values of \mathbf{D} . Diagonal

elements of Σ give a measure of the explained variance accounted by corresponding spatial pattern and time series. In the EEOF method, the extended data matrix, \mathbf{D}^E in equation (4.2) is decomposed by the SVD. Due to the configuration of \mathbf{D}^E , the elements in \mathbf{V} also include time-lagged information with the M month:

$$\mathbf{V} = \begin{bmatrix} v_1^1(1) & v_1^1(2) & \dots & v_1^1(M) & v_1^2(1) & \dots & v_1^j(t) & \dots & v_1^p(M) \\ \vdots & \vdots & \ddots & \vdots & \vdots & \ddots & \vdots & \ddots & \vdots \\ v_k^1(1) & v_k^1(2) & \dots & v_k^1(M) & v_k^2(1) & \dots & v_k^j(t) & \dots & v_k^p(M) \\ \vdots & \vdots & \ddots & \vdots & \vdots & \ddots & \vdots & \ddots & \vdots \end{bmatrix}^T, \quad (4.4)$$

where subscript and superscript indicate k th spatial mode and j th location index respectively, and t in parenthesis is a positive integer related with the *window length* parameter ranging from 1 to M . Therefore k th column of \mathbf{V} represents k th spatial mode and is rearranged for simplicity as follow:

$$\mathbf{V}_k = \left[\mathbf{v}_k^{(1,p)}(1) \quad \mathbf{v}_k^{(1,p)}(2) \quad \dots \quad \mathbf{v}_k^{(1,p)}(M) \right], \quad (4.5)$$

where $\mathbf{v}_k^{(1,p)}(t) = (v_k^1(t), v_k^2(t), \dots, v_k^j(t), \dots, v_k^p(t))^T$.

The EOF method can be used as a filter for a given data set by reconstruction with desired modes. The orthogonality of \mathbf{V} in equation (4.3) provides a complete basis for a given data set. In conventional EOF the reconstructed data set, \mathbf{D}' , can be described as

$$\mathbf{D}' = \sum_{k=1}^N \chi_k \sigma_k \mathbf{u}_k \mathbf{v}_k^T, \quad N = \min(n, p), \quad (4.6)$$

where \mathbf{u}_k and \mathbf{v}_k are k th column vectors of \mathbf{U} and \mathbf{V} respectively, and σ_k is k th diagonal element of Σ in equation (4.3). χ_k is a parameter to

determine which column vectors are included in the reconstruction. For example, if 1st and 3rd modes are used in the reconstructions, χ_1 and χ_3 are ones while others are zeros. If all χ_k are ones, the reconstructed \mathbf{D}' is equivalent to the initial data set, \mathbf{D} .

In the EEOF method, reconstruction is made by differently because its spatial modes include spatio-temporal variation as shown in equation (4.4). The reconstruction formula for EEOF is

$$\mathbf{D}' = \mathbf{M} \sum_{k=1}^N \chi_k \sigma_k \mathbf{u}_k * \mathbf{V}_k^T, \quad N = \min(m - M + 1, Mp), \quad (4.7)$$

where \mathbf{u}_k is k th column vector of \mathbf{U} in equation (4.3) with length of $(n - M + 1)$, and $*$ is a convolution operator applying on this vector. This operator converts the pre-vector (i.e. \mathbf{u}_k) to a Toeplitz matrix, enabling multiplication with following matrix:

$$\mathbf{u}_k * A = \begin{bmatrix} u_k^1 & 0 & \dots & 0 \\ u_k^2 & u_k^1 & \dots & \vdots \\ u_k^3 & u_k^2 & \dots & \vdots \\ \vdots & \vdots & \ddots & \vdots \\ 0 & 0 & \dots & u_k^{m-M+1} \end{bmatrix} A.$$

\mathbf{M} in equation (4.7) is the weighting diagonal matrix with $n \times n$ size. Since the extended data matrix, \mathbf{D}^E , has smaller contribution of the first and the last $M - 1$ months from the original data, the diagonal components of \mathbf{M} has $\text{diag}(1, 1/2, \dots, 1/(M - 1), 1/M, \dots, 1/M, 1/(M - 1), \dots, 1/2, 1)$.

4.3 Results

Two different ice mass variations in GrIS based on reduced GRACE data with and without the de-correlation process are first compared. The two cases represent current data processing strategies for the correlation error. Each method may have its merit and demerit. GRACE data after de-correlation filter is less contaminated by the error but a portion of signal is probably eliminated. Unfiltered GRACE data must preserve GrIS ice mass signal given temporal and spatial resolutions, but the signal is corrupted by the error. Comparisons between the two can underscore the influence of the correlation error into regional scale apparent ice mass variations in GrIS. For both cases, global SH coefficients are localized into GrIS regions with half degree buffer area to oceans [Harig and Simons, 2012].

Signal associated with ice mass change varies in seasonal and longer time scales while the correlation error would have shorter month-to-month variations because the error is associated with spatial aliasing of GRACE monthly sampling for sub-monthly gravity variations [Seo *et al.*, 2008]. On the other hand, for spatial variability, the longitudinal stripes of the error might not be clearly distinct from signal pattern of ice mass variations in GrIS since GrIS ice mass signal is mostly observed along the east and west coasts [Landerer and Swenson, 2012; Velicogna and Wahr, 2013]. Therefore, to compare any effect from the correlation error and signal loss via the de-correlation filter, it is necessary to examine spatio-temporal variations for the two cases. To this end, the GRACE data are represented by the hovmöller diagram, which is useful to highlight a spatio-

temporal variability at a given latitudinal or longitudinal band [*Roundy and Schreck III, 2009*]. The diagram stack apparent monthly ice mass variations along the $70 N^\circ$ in GrIS during the study period (2003-2014) (Figure 4.1a). Figures 4.1b-c are resulting diagrams associated with no de-correlation and de-correlation processes, respectively. Both show gradual changes from positive to negative anomalies from 2003 to 2014, indicating large ice mass decrease in west and east coast of Greenland [*Khan et al., 2015*]. However, they clearly exhibit signal loss and smoothing after de-correlation filter. Signal loss can be compensated by forward modeling in global SH [e.g., *Chen et al., 2013*], but signal smoothing issue is remained.

Because a strong negative trend (shown in Figures 4.1b-c) and annual cycle are well known signal variations in GrIS [*Wouters et al., 2008*], these components are removed from the apparent ice mass variations to examine residual smaller amplitude signal and errors from GRACE observations. Figures 4.1d-e are the similar diagrams to the Figures 4.1b-c, respectively, except that linear trends and seasonal cycles are eliminated. In general, both diagrams show an evident quadratic pattern in west coast and inter-annual variations in east coast. The distinct acceleration pattern and inter-annual variations are mainly associated with similar variations of accumulation of SMB [*Seo et al., 2015b*]. Figure 4.1e shows the similar signal smoothing to that shown in Figure 4.1c resulting from the de-correlation filter: the different ice mass variation patterns in west and east coasts are not clearly discernible. However, Figure 4.1d also suffers from abrupt month-to-month variations, which hamper understanding of small-scale ice mass variations. Therefore, both cases are not adequate to

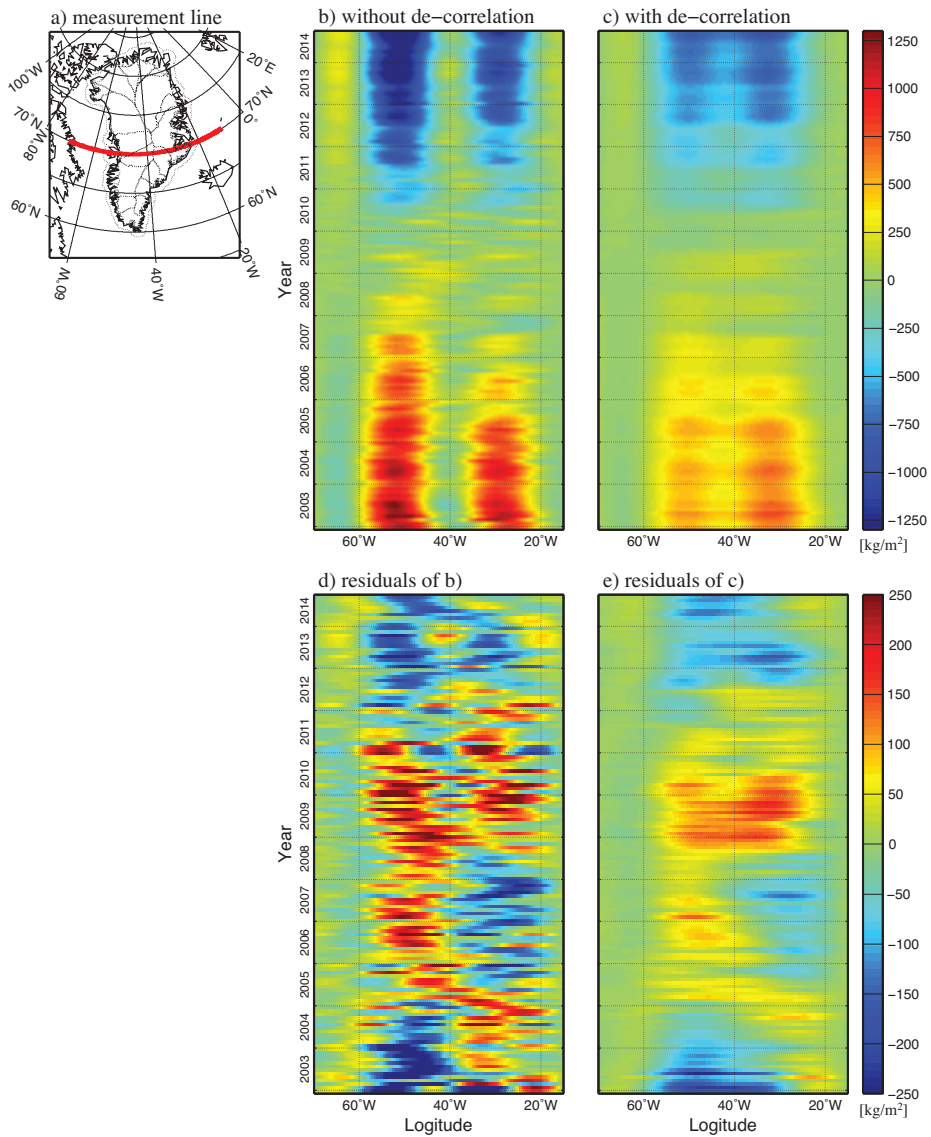


Figure 4.1 The hovmöller diagrams of ice mass variations for filtered and unfiltered GRACE data. a) marks measurement line on the map. b) and c) show the diagrams with and without de-correlation filter, respectively. d) and e) show residual diagrams after removing secular and seasonal variations.

infer regional scale ice mass variations from GRACE observations.

To exclude correlation error without signal loss and smoothing, the EEOF technique is applied on the localized SH coefficients. The *window length* is determined by 6 months to recover seasonal to sub-seasonal variations in the data. To reconstruct filtered data using EEOF, one determines signal and noise modes using visual examination of each spatial mode, \mathbf{V}_k . Since the longitudinal patterns from signal and errors in this region are mainly projected on higher order coefficients and the decomposition is also based on SH domain, the examination is performed on SH coefficients for a particular order as a function of degree. Then, those SH coefficients are stacked with respect to lagged time step, which is a similar hovmöller diagram in Figure 4.1b-e. Figure 4.2 shows first several hovmöller diagrams of different modes for an order 15. The horizontal axis of each panel refers to the degree of coefficient with positive sign representing the cosine coefficients and negative for the sine. The vertical axis indicates lagged time steps zero to 5 months. They have distinct patterns along the lagged time, which are partitioned by solid line. The coefficients in the first mode (Figure 4.2a) are time invariant. This feature of time independent coefficients is true for other orders for the first mode (not shown). This mode accounts for 92.8% of the total explained variance (EV), which indicates that most part of the total ice mass change in the Greenland can be represented by the first mode and arise in fixed location such as glacial outlets and areas yielding surface mass gain/loss in every year.

Figure 4.2b-g shows the modes whose coefficients gradually migrated

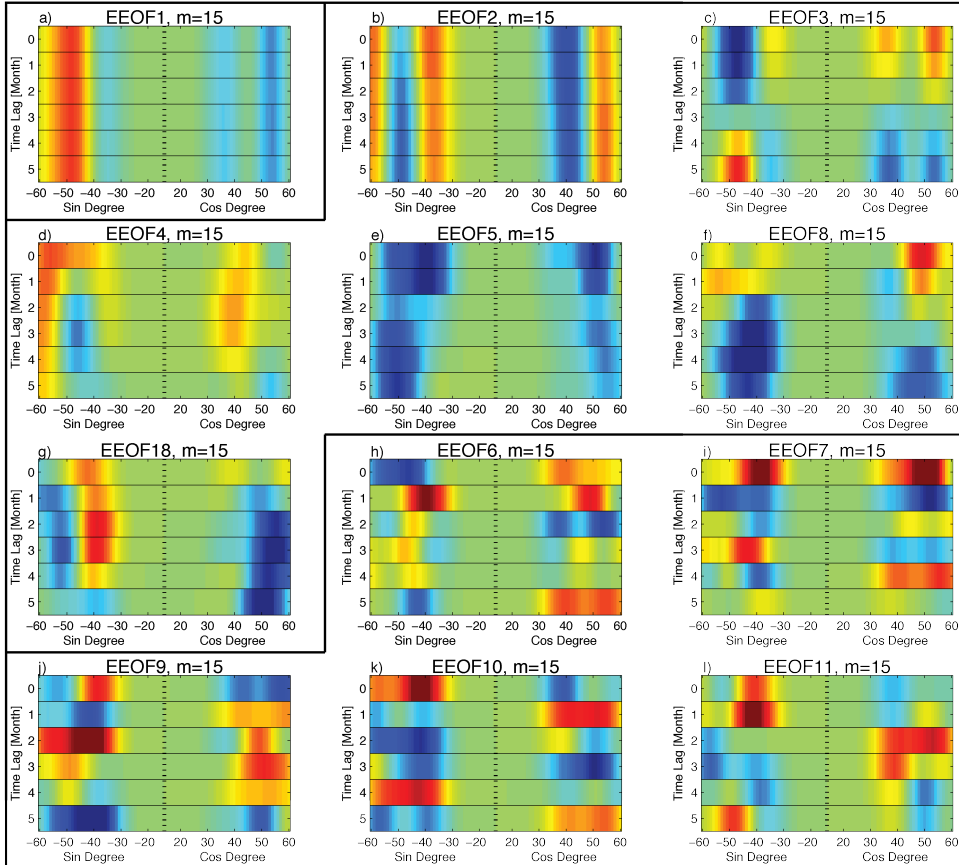


Figure 4.2 Hovmöller diagrams of different spatial modes for SH coefficients at order 15. The horizontal axis of each panel refers to the degree of coefficient with positive sign representing the cosine coefficients and negative for the sine. The vertical axis indicates lagged time steps from 0 to 5 months. Diagrams with distinct patterns along the lagged time are separated by solid black line. a) shows the time-invariable coefficients in the first mode. b-g) exhibit modes whose coefficients are gradually migrated with respect to time, while h-i) show modes which spatial patterns are randomly distributed.

as time passes. The EV of these modes is 3.8 %. The coefficients in latter modes including Figure 4.2h-l show random distribution. The total EV of these modes is 3.4 %, which is similar value to that of quasi-stationary modes. This indicates that the seasonal and inter-annual migration of regions producing ice mass variations can be described by a small fraction of total EV of the data, and thus it is very difficult to separate of this small signal from correlation error in a monthly GRACE solution. However, the EEOF decomposition technique could successfully distinguish signals associated with ice mass changes from correlation error using a coherent feature over time.

With recovered SH coefficients from EEOF decomposition by equation (4.7), ice mass variations are estimated over the GrIS and represented by the hovmöller diagram. Figure 4.3a is the similar to Figure 4.1b or 4.1c except that the diagram here is constructed from ice mass variations estimated by SH coefficients after EEOF. The diagram shows the evident linear trends at both coasts, but envelopes of anomalies are smoother than those shown in Figure 4.1b. As shown in Figures 4.1d-e, linear trends and seasonal cycles are removed from Figure 4.3a, and residual diagram is shown in Figure 4.3b. It clearly shows acceleration pattern in west and inter-annual variations in east similar to Figures 4.1d-e while the distinct spatial pattern between the west and east coasts are evident contrast to Figure 4.1d-e. As a result, EEOF method is likely effective to suppress the correlation error and possibly random noise with less signal smoothing and loss than the conventional de-correlation filter [*Swenson and Wahr, 2006*].

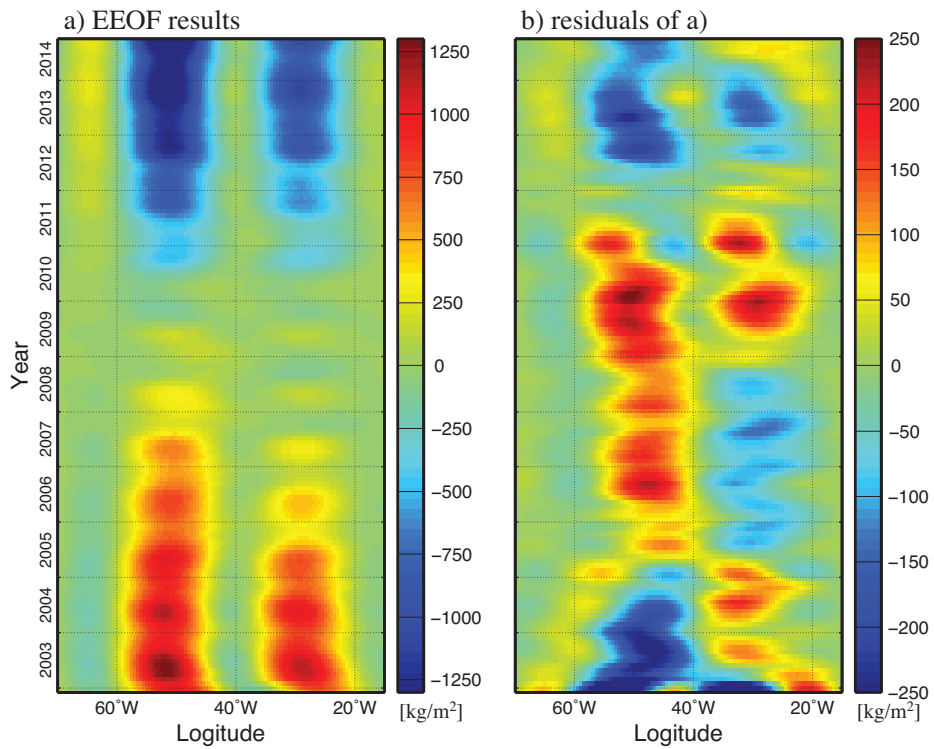


Figure 4.3 a) is the similar hovmöller diagrams to Figure 4.1a or 4.1b except that GRACE data is processed by EEOF. b) shows residual diagram after removing linear trends and seasonal cycles from a). It clearly shows acceleration pattern in west and inter-annual variations in east.

Further examination shows total GrIS ice mass variations integrated over the continent from the three different methods such as two cases of with and without de-correlation filter and EEOF. In Figure 4.4, gray and blue lines exhibit total GrIS ice mass variations from the localized SH coefficients that are calculated from global SH coefficients with and without the de-correlation procedure, respectively. The negative trend from the gray line is $-211.76 \pm 6.55 \text{ Gt/yr}$, which is about 20% smaller than that from the blue line, $-270.50 \pm 8.43 \text{ Gt/yr}$. On the other hand, the blue line shows high frequency month-to-month variations that are not shown in the gray line. The comparisons between the two time series indicate that unfiltered GRACE data over GrIS is probably corrupted by the de-correlation error, and filtered GRACE data is suffered from signal loss or smoothing [Velicogna and Wahr, 2013]. Signal smoothing into oceans is known as leakage error, and this is corrected via forward modeling [e.g., Chen et al., 2013]. However, the problem of the signal smoothing within GrIS as show in Figure 4.1c or 4.1e cannot be fixed. As an alternative, red line shows total GrIS mass variations from the localized SH coefficients after EEOF procedure. It shows similar trend to the blue line, $-270.43 \pm 7.90 \text{ Gt/yr}$, but the high frequency variations shown in the blue line is not evident. Consequently, results from Figures 4.3 and 4.4 indicate that EEOF method is effective to separate signal and de-correlation error (and possibly noise).

Additional experiment to examine the correlation error correction for the three different schemes is to compare their recoveries of GrIS mass variations to independent estimates. Because in-situ or remote sensing

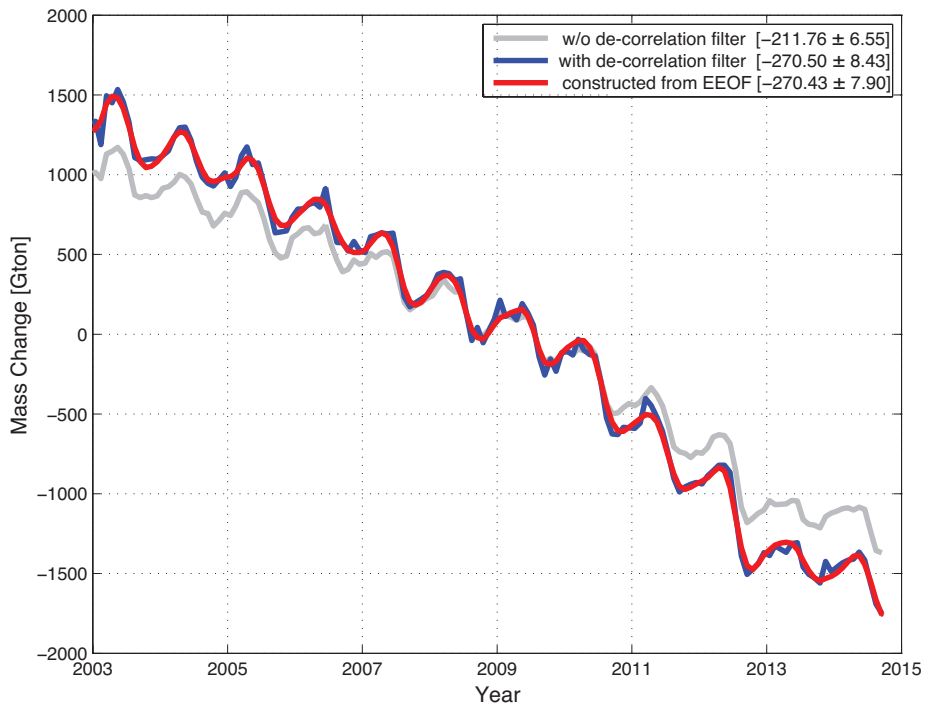


Figure 4.4 Basin average estimations for ice mass variations with (gray) and without (blue) de-correlation filter and EEOF (red). Included are linear trend estimates for each data set. All of them clearly show annual variations in total GrIS ice mass changes but different trends and month-to-month variations.

observations for GrIS that are comparable with GRACE observation are not available during the study period (2003-2014), SMB fields from regional climate model outputs (RACMO2.3) [Noël *et al.*, 2015] is used. Ice mass variations in ice sheet are determined by the difference between SMB and ice discharge into ocean:

$$\delta M = \int (SMB - D)dt = (SMB_0 - D_0)t + \int (\delta SMB - \delta D)dt, \quad (4.8)$$

where δM is an anomaly from the reference mass of ice sheet and SMB_0 and D_0 are the references of SMB and discharge, respectively [van den Broeke *et al.*, 2009]. By definition, SMB_0 and D_0 are equal, thus the first term on the far right hand side of equation (4.8) disappears. Accordingly, month-to-month ice mass variation in GrIS is described as follow:

$$\delta M_{t_1}^{t_2} = \int_{t_1}^{t_2} (\delta SMB - \delta D)dt, \quad (4.9)$$

where t_1 and t_2 denote adjacent two months. During winter in GrIS, ice discharge variations show annual minimum and almost constant [Bartholomew *et al.*, 2010; Joughin *et al.*, 2008; Rignot and Kanagaratnam, 2006]. Therefore, contribution of δD is very small in this period and the month-to-month ice mass variation is governed by SMB variations as follow:

$$\delta M_{t_2} - \delta M_{t_1} = [\delta SMB_{t_2} + \delta SMB_{t_1}]/2. \quad (4.10)$$

The anomalies δSMB are calculated from the RACMO2.3 after removing the reference value SMB_0 , which is a mean SMB values over GrIS during the study period (2003-2014) and is estimated as 248.6 Gt/yr.

Therefore, during winter, month-to-month GrIS mass variations observed by GRACE can be represented by SMB anomalies.

Comparisons between GRACE (δM) with RACMO2.3 (δSMB) are exhibited in Figure 4.5. Figures 4.5a-c show mean δSMB fields during adjacent two months from Nov. 2008 to Feb. 2009. It shows larger SMB increase from Nov. 2008 to Dec. 2008, and its increase was getting smaller until Jan. 2009. Figures 4.5d-f show the similar difference (δM) using GRACE data without applying the de-correlation filter. They clearly exhibit longitudinal stripes and are very different from SMB fields. Note that its scale is different from that in Figure 4.5a-c. Figures 4.5g-i shows cases after applying the de-correlation filter. At southern GrIS region, they show similar anomalies to the SMB (Figures 4.5a-c), but there are artifacts in northern part of the GrIS that are not exhibited in the SMB field. Finally, Figure 4.5j-l shows results after EEOF decomposition, and they are very close to the Figure 4.5a-c. This result confirms that EEOF method outperforms the conventional procedures for the correlation error and is useful to study regional ice mass variation in GrIS.

Since EEOF filtering is effective to suppress the correlation error with preserving ice mass signal, further examination is conducted for the month-to-month ice mass variations in GrIS with localized SH coefficients decomposed by EEOF. Figure 4.6 shows mean differences of ice mass variations between adjacent two months during the study period. For example, Figure 4.6a represents difference between mean ice mass variations in October and in September from 2003 to 2014. Figure 4.6 shows that ice mass variations are not apparent from September to November. How-

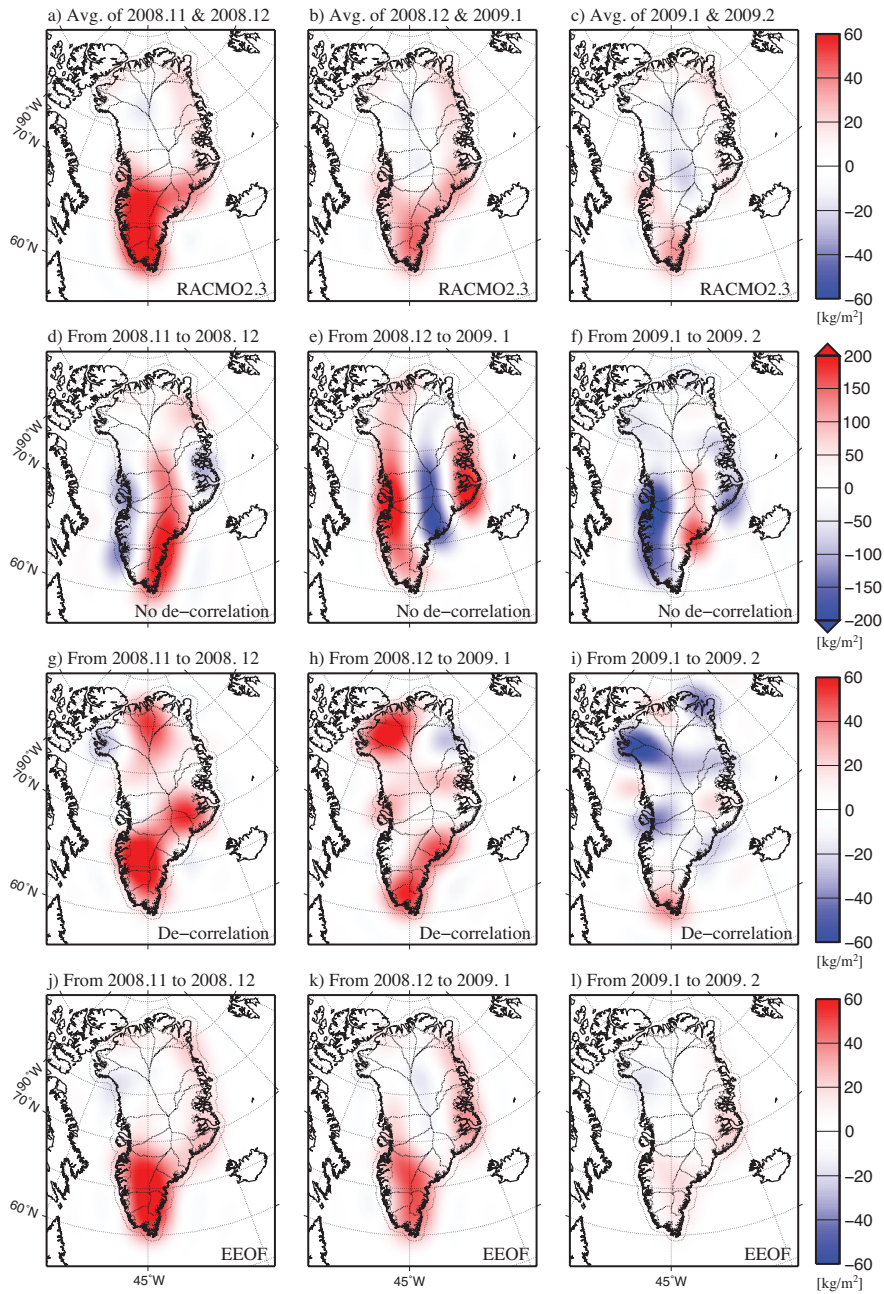


Figure 4.5 Comparisons of SMB fields calculated by RACMO2.3 (a-c) and consecutive month-to-month ice mass variations maps observed by GRACE without (d-f) and without de-correlation (g-i) and using EEOF (j-l).

ever, during winter (from November to March), ice mass accumulation is evident in southern part of the GrIS. Similar to the period of September to November, ice mass variations are not significant during spring seasons (from March to April). Finally, during summer (June to September), large ice mass loss is observed in the southern part of GrIS. In particular, difference maps during summer show that large negative anomalies are occurred at large glacial outlets such as Helheim and Kangerdlugssuaq in West coast and Jakobshavn Isbræ in the East [Howat *et al.*, 2011; Joughin *et al.*, 2010] due possibly to enhanced dynamical loss [Schoof, 2010]. Therefore, the significant negative anomaly along coastal regions during summer is likely due to ice mass loss associated with melting water runoff and enhanced ice discharge at the marine terminating glacial outlets. It is also important note that high altitude in-land regions show ice accumulation during summer.

GrIS mass loss associated with ice discharge can be estimated based on GRACE observations and SMB outputs from the regional climate model using equation (4.9), and it is compared with a previous ice discharge estimate determined by ice thickness and velocity survey [Enderlin *et al.*, 2014]. They found that the total discharge during 10 years (2003-2012) was 5,231 Gt . Based on equation (4.9) from the GRACE observations after EEOF filtering and SMB, ice discharge anomaly (δD) to GrIS mass changes is 2,517 Gt . With consideration of the reference ice discharge ($D_0 = 248.6 Gt/yr$), the total mass loss due to the ice discharge from 2003 to 2012 is 5,003 Gt , which is very close to the previous estimate.

In addition, Figure 4.7 shows a map of GrIS ice mass loss associated

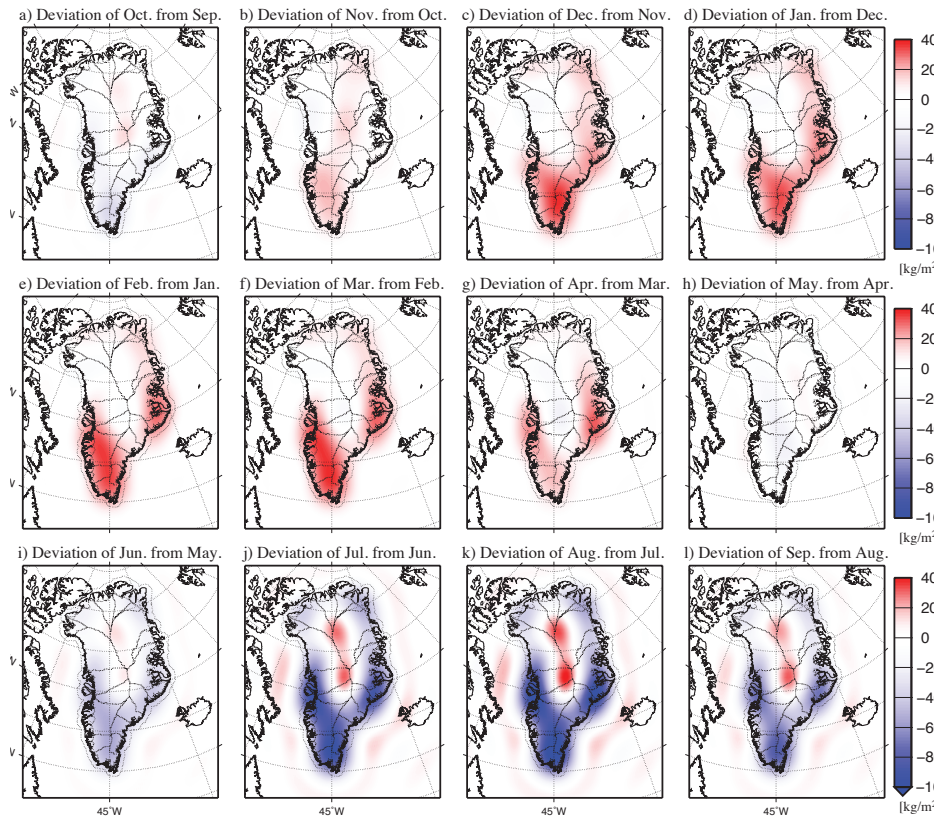


Figure 4.6 Mean monthly difference maps of ice mass from 2003 to 2014.

with ice discharge. Large ice mass loss appears in the western, southeastern and northeastern coastal regions. This spatial pattern and amplitude of ice mass loss also agree with a previous estimate (Figure 4.8) based on satellite remote sensing [Enderlin *et al.*, 2014]. Figure 4.8 shows locations of 178 marine-terminating outlet glaciers with termini width larger than 1 km and their ice discharge amplitudes during 2003-2012. Most ice discharge in GrIS has occurred in southeast and west coastal regions that agree well with GRACE-based estimate shown in Figure 4.7.

4.4 Discussion

Mass changes estimation from the GRACE solutions has conventionally faced the problem of achieving effective error removal with minimal loss of signal. The longitudinal errors in the high degree and order SH coefficients are problematic to appraise accurate seasonal mass variations. To suppress the errors, many GRACE applications have adopted the decorrelation filter which removes correlated variations of SH coefficients. Although the procedure is fairly effective, the resulting loss of signal and smoothing, particularly in GrIS, are often significant.

In this chapter, the design of a novel method to remove the errors is presented. The EEOF method decomposes the monthly GRACE data in SH domain with consideration of time-lagged information and then reconstructs correlation-free data set by gathering modes exhibiting gradual time migration. In comparison of month-to-month variations, the EEOF method retrieves SMB field of GrIS successfully, which agrees remarkably well with the regional climate model, while GRACE data reduction with

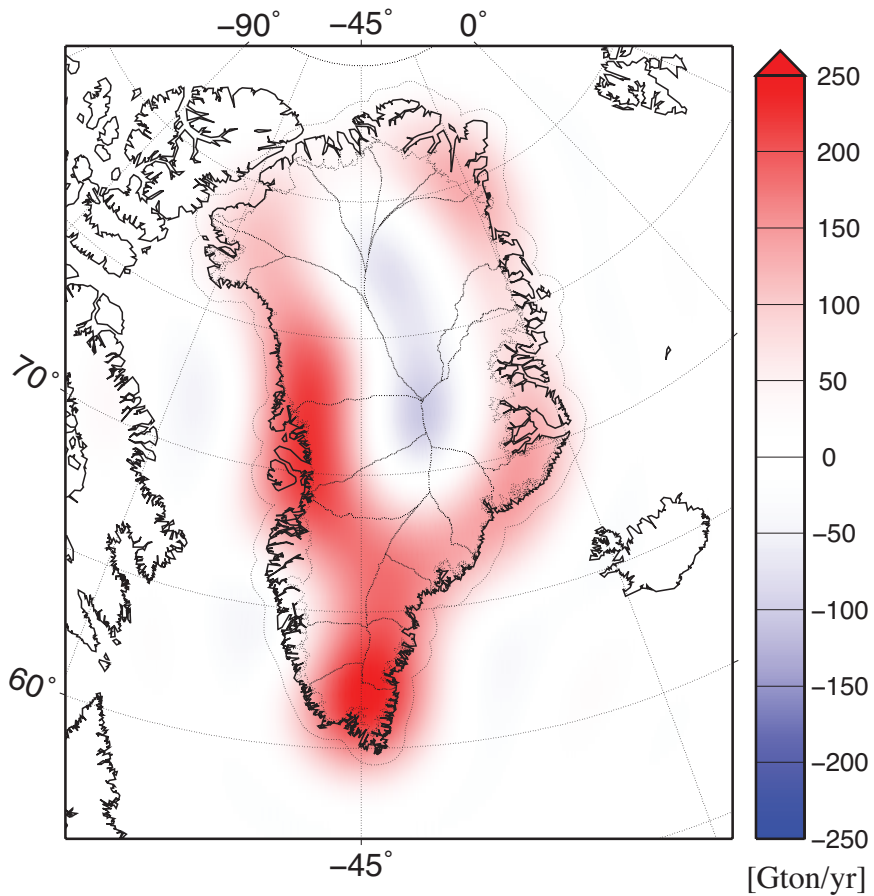


Figure 4.7 Ice discharge map of GrIS recovered from GRACE and RACMO2.3. Large ice mass loss appears in the western, southeastern and northeastern coastal regions. This spatial pattern and amplitude of ice mass loss also agree with a previous estimate based on satellite remote sensing.

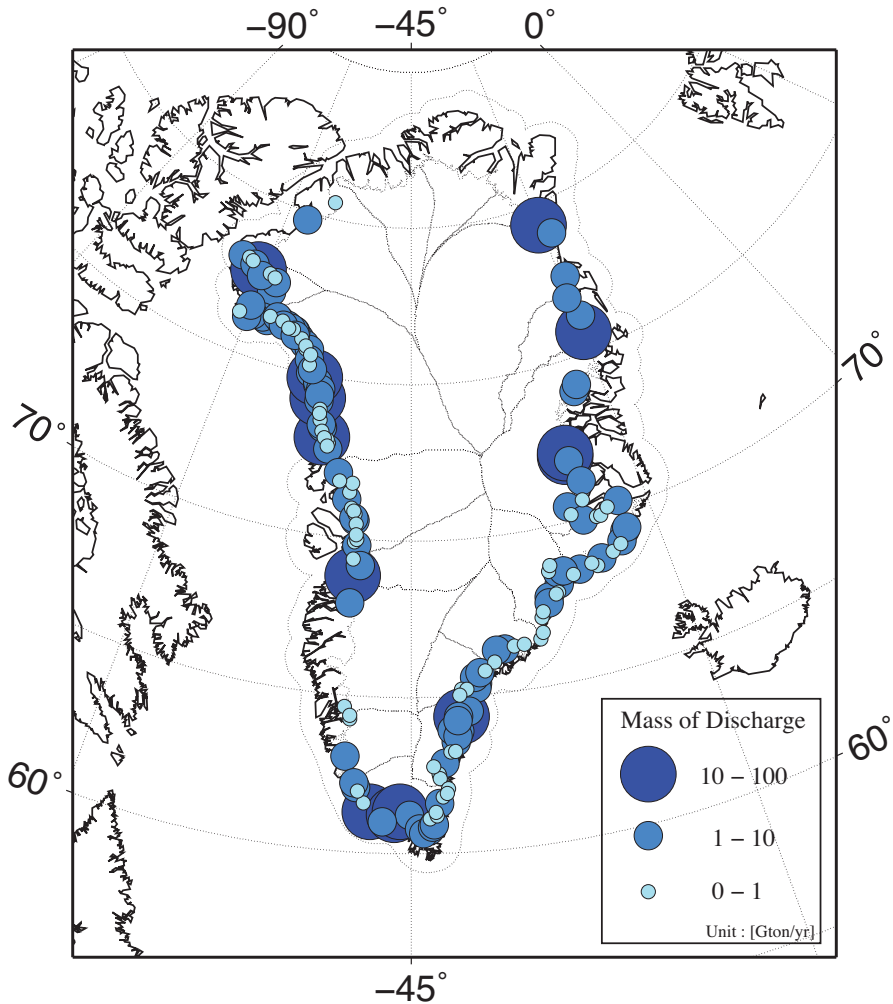


Figure 4.8 Locations and amplitude of 178 marine-terminating outlet glaciers with termini width larger than 1 km. Most ice discharge in GrIS was occurred in southeast and west coastal regions that agree well with GRACE-based estimate shown in Figure 4.7.

and without the de-correlation process show significant signal loss and longitudinal stripes, respectively.

The prominent advantage of EEOF over the de-correlation filter is that the EEOF can recover seasonal mass change in GrIS. Previous applications by conventional procedures of error reduction are limited to long-term estimation of GrIS mass change because the procedures diminish the information about the seasonal variations with reducing errors. The EEOF technique can successfully separate signals related with GrIS mass change and provide accurate mass variation of GrIS in seasonal and regional scale. Consequently, for the first time, annual maps of month-to-month mass variations in GrIS can be presented from the GRACE, and they agree with other independent studies.

Ice discharge map recovered from GRACE and RACMO2.3, as shown in Figure 4.7, represents opposite sign in the central region implying slight mass gain during summer. The increase can be explained by one (or more) of three reasons: 1. The high anomaly in coastal region due to ice discharge induce apparent negative ripples in the representation of limited SH coefficients, 2. RACMO2.3 has under-estimated the accumulation of mass in the region and/or 3. The ice flow velocity in the central GrIS has decreased thus resulting increase of ice thickness. Further study is required to determine which cause contributes to the opposite anomaly in the central region.

In combination with estimation of surface meltwater penetration and icesheet velocity data, the GRACE results from the EEOF is expected to provide knowledge of subglacial hydrologic system and thus further

contributes to resolve the mechanism of ice loss in GrIS.

Chapter 5. Conclusions

In this dissertation, surface water mass variations are examined in the Amazon Basin (Chapter 3) and the GrIS (Chapter 4) using monthly GRACE gravity data. Difficulty in recovery of surface mass variations from GRACE lies in GRACE error reduction with least signal loss, especially at sub-basin spatial scale. EOF decomposition is useful to separate signals associated with water mass change from errors in GRACE data. However, this technique focuses to maximize variance of decomposed modes, so physical interpretation for each mode is restricted. Therefore, the modified EOF methods are adopted to overcome this limitation. In Amazon Basin, the rotated EOF (REOF) method is used to recover TWS changes from main channel because REOF can isolate TWS signals having a same phase with a river discharge variations into a single mode while conventional EOF projects the main channel signals into multiple modes. In Greenland, GRACE aliasing error has the similar spatial pattern to ice mass variations. As a result, conventional EOF cannot distinguish signal and error. The extended EOF (EEOF), on the other hand, considers spatial and temporal correlation simultaneously, and thus can reduce aliasing error significantly with least signal loss.

The major findings in this study are as follows:

1. Comparisons between in-situ river discharge and estimated river discharge based on REOF at Óbidos station shows significant discrepan-

cies during high water seasons while the two time series agrees remarkably during other seasons. This result represents that total river discharge of the basin is not probably gauged by in-situ observations during high water season. During flooding, a large amount of water mass detours around the Óbidos station by flowing through complex channels temporally developed in a huge flood plain at south of main stem. In GRACE-based analysis, the water volume detouring gauge is about 6 % of annual discharge of the basin in 2009.

2. REOF method does not require in-situ observations for estimate discharge. This advantage allows the method to extend for large basin where in-situ observations are limited at their basin mouth. In this study, the method is applied to entire Amazon Basin whose total river discharge has been unknown due to complex channel structure and ocean tidal effect. The result shows an enormous amount of monthly discharge, 1,050 Gt, was occurred during June 2009.

3. For GrIS ice mass change, the EEOF provides much superior results to filtered and unfiltered GRACE data, which are two conventional GRACE data processing methods in the region. Filtered GRACE data after de-correlation filter shows significant signal loss, so it is not clear to identify ice mass gain/loss. Noisy mass variations in spatial distribution and amplitude are also found in month-to-month mass changes from unfiltered GRACE data due to aliasing effect. On the other hand, a reasonable month-to-month mass distribution map can be obtained by EEOF application. During winter season, when SMB is a major contributor to mass changes in GrIS, results of EEOF remarkably agree with

outputs of regional climate model, RACMO2.3 in amplitude and spatial distribution.

4. The successful recovery of ice mass variation in GrIS from GRACE data, in particular near the coastal regions, can be used to identify mass loss distribution due to ice discharge. Large amount of mass loss and gain in GrIS is associated with SMB. Difference between EEOF results from GRACE (total mass loss) and SMB provides ice discharge contribution to ice mass loss. The spatial distribution of the estimated ice mass loss associated with ice discharge is remarkably consistent with results of *Enderlin et al.* [2014], which were obtained by ice thickness and velocity surveys, independent with GRACE observation.

References

- A, G., J. Wahr, and S. Zhong, 2013, Computations of the viscoelastic response of a 3-D compressible Earth to surface loading: an application to Glacial Isostatic Adjustment in Antarctica and Canada, *Geophysical Journal International*, 192(2), 557–572, doi:10.1093/gji/ggs030.
- Alsdorf, D. E., and D. P. Lettenmaier, 2003, Tracking fresh water from space, *Science*, 301(5639), 1491–1494, doi:10.1126/science.1089802.
- Alsdorf, D. E., E. Rodriguez, and D. P. Lettenmaier, 2007, Measuring surface water from space, *Reviews of Geophysics*, 45(2), doi:10.1029/2006rg000197.
- Alsdorf, D. E., S. C. Han, P. Bates, and J. Melack, 2010, Seasonal water storage on the Amazon floodplain measured from satellites, *Remote Sensing of Environment*, 114(11), 2448–2456, doi:10.1016/J.Rse.2010.05.020.
- Bartholomew, I., P. Nienow, D. Mair, A. Hubbard, M. A. King, and A. Sole, 2010, Seasonal evolution of subglacial drainage and acceleration in a Greenland outlet glacier, *Nature Geosci*, 3(6), 408–411, doi:10.1038/ngeo863.
- Bettadpur, S., 2012, CSR level-2 processing standards document for level-2 product release 05.
- Bjerklie, D. M., S. L. Dingman, C. J. Vorosmarty, C. H. Bolster, and R. G. Congalton, 2003, Evaluating the potential for measuring river

discharge from space, *Journal of Hydrology*, 278(1–4), 17 – 38, doi:
[http://dx.doi.org/10.1016/S0022-1694\(03\)00129-X](http://dx.doi.org/10.1016/S0022-1694(03)00129-X).

Bonan, G. B., 1998, The land surface climatology of the NCAR land surface model coupled to the NCAR community climate model*, *Journal of Climate*, 11(6), 1307–1326.

Cazenave, A., and J. Chen, 2010, Time-variable gravity from space and present-day mass redistribution in the Earth system, *Earth and Planetary Science Letters*, 298(3–4), 263 – 274, doi:
[10.1016/j.epsl.2010.07.035](https://doi.org/10.1016/j.epsl.2010.07.035).

Chambers, D. P., 2006, Evaluation of new GRACE time-variable gravity data over the ocean, *Geophys. Res. Lett.*, 33, L17603, doi:
[10.1029/2006gl027296](https://doi.org/10.1029/2006gl027296).

Chen, J., C. Wilson, J. Famiglietti, and M. Rodell, 2007, Attenuation effect on seasonal basin-scale water storage changes from GRACE time-variable gravity, *Journal of Geodesy*, 81(4), 237–245, doi:
[10.1007/s00190-006-0104-2](https://doi.org/10.1007/s00190-006-0104-2).

Chen, J. L., C. R. Wilson, and B. D. Tapley, 2011, Interannual variability of Greenland ice losses from satellite gravimetry, *J. Geophys. Res.*, 116, B07406, doi:[10.1029/2010jb007789](https://doi.org/10.1029/2010jb007789).

Chen, J. L., C. R. Wilson, and B. D. Tapley, 2013, Contribution of ice sheet and mountain glacier melt to recent sea level rise, *Nature Geosci.*, 6(7), 549–552, doi:[10.1038/ngeo1829](https://doi.org/10.1038/ngeo1829).

- Cheng, M., and B. D. Tapley, 2004, Variations in the Earth's oblateness during the past 28 years, *Journal of Geophysical Research: Solid Earth*, *109*, B09402, doi:10.1029/2004JB003028.
- Dee, D. P., S. M. Uppala, A. J. Simmons, P. Berrisford, P. Poli, S. Kobayashi, U. Andrae, M. A. Balmaseda, G. Balsamo, P. Bauer, P. Bechtold, A. C. M. Beljaars, L. van de Berg, J. Bidlot, N. Bormann, C. Delsol, R. Dragani, M. Fuentes, A. J. Geer, L. Haimberger, S. B. Healy, H. Hersbach, E. V. Hólm, L. Isaksen, P. Kállberg, M. Köhler, M. Matricardi, A. P. McNally, B. M. Monge-Sanz, J.-J. Morcrette, B.-K. Park, C. Peubey, P. de Rosnay, C. Tavolato, J.-N. Thépaut, and F. Vitart, 2011, The ERA-interim reanalysis: configuration and performance of the data assimilation system, *Quarterly Journal of the Royal Meteorological Society*, *137*(656), 553–597, doi:10.1002/qj.828.
- Di Baldassarre, G., and P. Claps, 2010, A hydraulic study on the applicability of flood rating curves, *Hydrology Research*, *42*(1), 10–19.
- Di Baldassarre, G., and A. Montanari, 2009, Uncertainty in river discharge observations: a quantitative analysis, *Hydrol. Earth Syst. Sci.*, *13*(6), 913–921, doi:10.5194/hess-13-913-2009, hESS.
- Dickey, J. O., et al., 1997, *Satellite Gravity and the Geosphere: Contributions to the Study of the Solid Earth and Its Fluid Envelopes*, The National Academies Press, Washington, DC, doi:10.17226/5767.
- Enderlin, E. M., I. M. Howat, S. Jeong, M.-J. Noh, J. H. van Angelen, and M. R. van den Broeke, 2014, An improved mass budget for the

Greenland ice sheet, *Geophysical Research Letters*, 41(3), 866–872, doi: 10.1002/2013GL059010.

Espinoza, J. C., J. L. Guyot, J. Ronchail, G. Cochonneau, N. Filizola, P. Fraizy, D. Labat, E. de Oliveira, J. J. Ordoñez, and P. Vauchel, 2009, Contrasting regional discharge evolutions in the Amazon basin (1974–2004), *Journal of Hydrology*, 375, 297 – 311, doi: 10.1016/j.jhydrol.2009.03.004.

Farrell, W. E., 1972, Deformation of the Earth by surface loads, *Reviews of Geophysics*, 10(3), 761–797, doi:10.1029/RG010i003p00761.

Farrell, W. E., and J. A. Clark, 1976, On postglacial sea level, *Geophysical Journal International*, 46(3), 647–667, doi:10.1111/j.1365-246X.1976.tb01252.x.

Filizola, N., E. M. Latrubesse, P. Fraizy, R. Souza, V. Guimarães, and J.-L. Guyot, 2014, Was the 2009 flood the most hazardous or the largest ever recorded in the Amazon?, *Geomorphology*, 215, 99 – 105, doi: 10.1016/j.geomorph.2013.05.028.

Frappart, F., L. Seoane, and G. Ramillien, 2013, Validation of GRACE-derived terrestrial water storage from a regional approach over South America, *Remote Sensing of Environment*, 137, 69 – 83, doi: 10.1016/j.rse.2013.06.008.

Han, S.-C., C. K. Shum, C. Jekeli, C.-Y. Kuo, C. Wilson, and K.-W. Seo, 2005, Non-isotropic filtering of GRACE temporal gravity for geophysi-

cal signal enhancement, *Geophysical Journal International*, 163(1), 18–25, doi:10.1111/j.1365-246X.2005.02756.x.

Han, S.-C., I.-Y. Yeo, D. Alsdorf, P. Bates, J.-P. Boy, H. Kim, T. Oki, and M. Rodell, 2010, Movement of Amazon surface water from time-variable satellite gravity measurements and implications for water cycle parameters in land surface models, *Geochem. Geophys. Geosyst.*, 11(9), doi:10.1029/2010GC003214.

Hannachi, A., I. T. Jolliffe, and D. B. Stephenson, 2007, Empirical orthogonal functions and related techniques in atmospheric science: A review, *International Journal of Climatology*, 27(9), 1119–1152, doi:10.1002/joc.1499.

Harig, C., and F. J. Simons, 2012, Mapping Greenland's mass loss in space and time, *Proc. Natl. Acad. Sci. U.S.A.*, 109(49), 19934–19937, doi:10.1073/pnas.1206785109.

Herschy, R. W., 2009, *Streamflow Measurement*, CRC Press, London, accession Number: 232640. Edition: 3rd ed.

Howat, I. M., Y. Ahn, I. Joughin, M. R. van den Broeke, J. T. M. Lenaerts, and B. Smith, 2011, Mass balance of Greenland's the largest outlet glaciers, 2000-2010, *Geophysical Research Letters*, 38, L12501, doi:10.1029/2011GL047565.

IPCC, 2014, Mitigation of Climate Change. Contribution of Working Group III to the Fifth Assessment Report of the Intergovernmental Panel on Climate Change. Contribution of

Working Group III to the Fifth Assessment Report of the Intergovernmental Panel on Climate Change, *Cambridge, United Kingdom and New York, USA*.

Jalbert, J., T. Mathevet, and A.-C. Favre, 2011, Temporal uncertainty estimation of discharges from rating curves using a variographic analysis, *Journal of Hydrology*, 397(1–2), 83 – 92, doi: 10.1016/j.jhydrol.2010.11.031.

Jolliffe, I. T., 2002, *Principal Component Analysis and Factor Analysis*, Springer Series in Statistics, 150-166 pp., Springer New York.

Joughin, I., S. B. Das, M. A. King, B. E. Smith, I. M. Howat, and T. Moon, 2008, Seasonal speedup along the Western flank of the Greenland ice sheet, *Science*, 320(5877), 781–783, doi: 10.1126/science.1153288.

Joughin, I., B. E. Smith, I. M. Howat, T. Scambos, and T. Moon, 2010, Greenland flow variability from ice-sheet-wide velocity mapping, *Journal of Glaciology*, 56(197), 415–430, doi:10.3189/002214310792447734.

Kaula, W. M., 1966, *Theory of satellite geodesy: applications of satellites to geodesy*, 120 pp., Blaisdell, Waltham, Mass.

Khan, S. A., A. Aschwanden, A. A. Bjørk, J. Wahr, K. K. Kjeldsen, and K. H. Kjær, 2015, Greenland ice sheet mass balance: A review, *Reports on Progress in Physics*, 78(4), 046,801.

Klees, R., E. A. Revtova, B. C. Gunter, P. Ditmar, E. Oudman, H. C. Winsemius, and H. H. G. Savenije, 2008, The design of an optimal

filter for monthly GRACE gravity models, *Geophysical Journal International*, 175(2), 417–432, doi:10.1111/j.1365-246X.2008.03922.x.

Knutti, R., J. Fluckiger, T. F. Stocker, and A. Timmermann, 2004, Strong hemispheric coupling of glacial climate through freshwater discharge and ocean circulation, *Nature*, 430(7002), 851–856, doi: 10.1038/nature02786, 10.1038/nature02786.

Kostaschuk, R., P. Villard, and J. Best, 2004, Measuring velocity and shear stress over dunes with acoustic doppler profiler, *Journal of Hydraulic Engineering*, 130(9), 932–936, doi:10.1061/(ASCE)0733-9429(2004)130:9(932).

Kosuth, P., J. Callède, and A. Laraque, 2000, Ocean tide waves propagation along downstream Amazon River: measuring the Amazon discharge at the estuary, pp. 1–10, *American Society of Civil Engineers*, doi:10.1061/40517(2000)310 10.1061/40517(2000)310.

Kouraev, A. V., E. A. Zakharova, O. Samain, N. M. Mognard, and A. Cazenave, 2004, Ob' river discharge from TOPEX/Poseidon satellite altimetry (1992–2002), *Remote Sensing of Environment*, 93(1–2), 238 – 245, doi:10.1016/j.rse.2004.07.007.

Landerer, F. W., and S. C. Swenson, 2012, Accuracy of scaled GRACE terrestrial water storage estimates, *Water Resources Research*, 48, W04531, doi:10.1029/2011WR011453.

Lang, M., K. Pobanz, B. Renard, E. Renouf, and E. Sauquet, 2010, Extrapolation of rating curves by hydraulic modelling, with application

to flood frequency analysis, *Hydrological Sciences Journal*, 55(6), 883–898, doi:10.1080/02626667.2010.504186.

Leon, J., S. Calmant, F. Seyler, M.-P. Bonnet, M. Cauhopé, F. Frappart, N. Filizola, and P. Fraizy, 2006, Rating curves and estimation of average water depth at the upper Negro River based on satellite altimeter data and modeled discharges, *Journal of Hydrology*, 328(3–4), 481 – 496.

Leonard, J., M. Mietton, H. Najib, and P. Gourbesville, 2000, Rating curve modelling with Manning’s equation to manage instability and improve extrapolation, *Hydrological Sciences Journal*, 45(5), 739–750, doi:10.1080/02626660009492374.

Liston, G. E., Y. C. Sud, and E. F. Wood, 1994, Evaluating GCM land surface hydrology parameterizations by computing river discharges using a runoff routing model: Application to the Mississippi Basin, *Journal of Applied Meteorology*, 33(3), 394–405, doi:10.1175/1520-0450.

Longuevergne, L., B. R. Scanlon, and C. R. Wilson, 2010, GRACE hydrological estimates for small basins: evaluating processing approaches on the High Plains Aquifer, USA, *Water Resources Research*, 46(11), doi:10.1029/2009WR008564.

Marengo, J., 2005, Characteristics and spatio-temporal variability of the Amazon River Basin water budget, *Climate Dynamics*, 24(1), 11–22, doi:10.1007/s00382-004-0461-6.

Marengo, J., J. Tomasella, W. Soares, L. Alves, and C. Nobre, 2012,

- Extreme climatic events in the Amazon Basin, *Theoretical and Applied Climatology*, 107(1-2), 73–85, doi:10.1007/s00704-011-0465-1.
- Milly, P. C. D., R. T. Wetherald, K. A. Dunne, and T. L. Delworth, 2002, Increasing risk of great floods in a changing climate, *Nature*, 415(6871), 514–517, 10.1038/415514a.
- Moon, T., I. Joughin, B. Smith, M. R. van den Broeke, W. J. van de Berg, B. Noël, and M. Usher, 2014, Distinct patterns of seasonal Greenland glacier velocity, *Geophysical Research Letters*, 41(20), 7209–7216, doi: 10.1002/2014GL061836.
- Navarra, A., and V. Simoncini, 2010, *A Guide to Empirical Orthogonal Functions for Climate Data Analysis*, Springer Netherlands.
- Noël, B., W. J. van de Berg, E. van Meijgaard, P. Kuipers Munneke, R. S. W. van de Wal, and M. R. van den Broeke, 2015, Summer snowfall on the Greenland Ice Sheet: a study with the updated regional climate model RACMO2.3, *The Cryosphere Discussions*, 9(1), 1177–1208, doi: 10.5194/tcd-9-1177-2015.
- Nohara, D., A. Kitoh, M. Hosaka, and T. Oki, 2006, Impact of climate change on river discharge projected by multimodel ensemble, *Journal of Hydrometeorology*, 7(5), 1076–1089, doi:10.1175/JHM531.1.
- Oki, T., T. Nishimura, and P. Dirmeyer, 1999, Assessment of annual runoff from land surface models using total runoff integrating pathways (trip), *Journal of the Meteorological Society of Japan. Ser. II*, 77(1B), 235–255.

- Oltman, R. E., 1968, *Reconnaissance investigations of the discharge and water quality of the Amazon River*, vol. 552, US Government Printing Office.
- Petersen-Øverleir, A., and T. Reitan, 2009, Accounting for rating curve imprecision in flood frequency analysis using likelihood-based methods, *Journal of Hydrology*, *366*(1–4), 89–100, doi:10.1016/j.jhydrol.2008.12.014.
- Richey, J. E., C. Nobre, and C. Deser, 1989, Amazon River discharge and climate variability: 1903 to 1985, *Science*, *246*(4926), 101–103, doi:10.2307/1703919.
- Riegger, J., and M. J. Tourian, 2014, Characterization of runoff-storage relationships by satellite gravimetry and remote sensing, *Water Resources Research*, *50*(4), 3444–3466, doi:10.1002/2013wr013847.
- Rignot, E., and P. Kanagaratnam, 2006, Changes in the velocity structure of the Greenland ice sheet, *Science*, *311*(5763), 986–990, doi:10.1126/science.1121381.
- Rignot, E., and J. Mouginot, 2012, Ice flow in Greenland for the International Polar Year 208–2009, *Geophysical Research Letters*, *39*, L11501, doi:10.1029/2012GL051634.
- Rignot, E., I. Velicogna, M. R. van den Broeke, A. Monaghan, and J. T. M. Lenaerts, 2011, Acceleration of the contribution of the Greenland and Antarctic ice sheets to sea level rise, *Geophysical Research Letters*, *38*(5), L05,503, doi:10.1029/2011GL046583.

- Rodell, M., P. R. Houser, U. Jambor, J. Gottschalck, K. Mitchell, C. J. Meng, K. Arsenault, B. Cosgrove, J. Radakovich, M. Bosilovich, J. K. Entin*, J. P. Walker, D. Lohmann, and D. Toll, 2004, The global land data assimilation system, *Bulletin of the American Meteorological Society*, 85(3), 381–394, doi:10.1175/BAMS-85-3-381.
- Roundy, P. E., and C. J. Schreck III, 2009, A combined wave-number-frequency and time-extended EOF approach for tracking the progress of modes of large-scale organized tropical convection, *Quarterly Journal of the Royal Meteorological Society*, 135(638), 161–173, doi:10.1002/qj.356.
- Rudorff, C. M., J. M. Melack, and P. D. Bates, 2014, Flooding dynamics on the lower Amazon floodplain: 1. Hydraulic controls on water elevation, inundation extent, and river-floodplain discharge, *Water Resources Research*, 50(1), 619–634, doi:10.1002/2013WR014091.
- Schmidt, R., F. Flechtner, U. Meyer, K.-H. Neumayer, C. Dahle, R. König, and J. Kusche, 2008, Hydrological signals observed by the GRACE satellites, *Surveys in Geophysics*, 29(4-5), 319–334, doi:10.1007/s10712-008-9033-3.
- Schoof, C., 2010, Ice-sheet acceleration driven by melt supply variability, *Nature*, 468(7325), 803–806, doi:10.1038/nature09618.
- Schrama, E. J. O., and B. Wouters, 2011, Revisiting Greenland ice sheet mass loss observed by GRACE, *Journal of Geophysical Research: Solid Earth*, 116, B02407, doi:10.1029/2009JB006847.

- Schrama, E. J. O., B. Wouters, and D. A. Lavallée, 2007, Signal and noise in Gravity Recovery and Climate Experiment (GRACE), *Journal of Geophysical Research: Solid Earth*, 112, B08407, doi:10.1029/2006JB004882.
- Schrama, E. J. O., B. Wouters, and R. Rietbroek, 2014, A mascon approach to assess ice sheet and glacier mass balances and their uncertainties from GRACE data, *Journal of Geophysical Research: Solid Earth*, 119(7), 6048–6066, doi:10.1002/2013JB010923.
- Seo, K.-W., and C. R. Wilson, 2005, Simulated estimation of hydrological loads from GRACE, *Journal of Geodesy*, 78(7-8), 442–456, doi:10.1007/s00190-004-0410-5.
- Seo, K.-W., C. R. Wilson, J. Chen, and D. E. Waliser, 2008, GRACE's spatial aliasing error, *Geophysical Journal International*, 172(1), 41–48, doi:10.1111/j.1365-246X.2007.03611.x.
- Seo, K.-W., C. R. Wilson, T. Scambos, B.-M. Kim, D. E. Waliser, B. Tian, B.-H. Kim, and J. Eom, 2015a, Surface mass balance contributions to acceleration of antarctic ice mass loss during 2003–2013, *Journal of Geophysical Research: Solid Earth*, 120(5), 3617–3627, doi:10.1002/2014JB011755.
- Seo, K.-W., D. E. Waliser, C.-K. Lee, B. Tian, T. Scambos, B.-M. Kim, J. H. van Angelen, and M. R. van den Broeke, 2015b, Accelerated mass loss from Greenland ice sheet: Links to atmospheric circulation

in the North Atlantic, *Global and Planetary Change*, 128, 61 – 71, doi: 10.1016/j.gloplacha.2015.02.006.

Shabalova, M. V., W. P. van Deursen, and T. A. Buishand, 2003, Assessing future discharge of the river Rhine using regional climate model integrations and a hydrological model, *Climate Research*, 23(3), 233–246.

Sheffield, J., C. R. Ferguson, T. J. Troy, E. F. Wood, and M. F. McCabe, 2009, Closing the terrestrial water budget from satellite remote sensing, *Geophysical Research Letters*, 36(7), doi:10.1029/2009GL037338.

Shiklomanov, A. I., R. B. Lammers, and C. J. Vörösmarty, 2002, Widespread decline in hydrological monitoring threatens Pan-Arctic Research, *Eos, Transactions American Geophysical Union*, 83(2), 13–17, doi:10.1029/2002EO000007.

Simpson, M. R., and R. N. Oltmann, 1993, *Discharge-measurement system using an Acoustic Doppler Current Profiler with applications to large rivers and estuaries*, US Government Printing Office.

Smith, L. C., 1997, Satellite remote sensing of river inundation area, stage, and discharge: A review, *Hydrological Processes*, 11(10), 1427–1439.

Swenson, S., and J. Wahr, 2002, Methods for inferring regional surface-mass anomalies from Gravity Recovery and Climate Experiment (GRACE) measurements of time-variable gravity, *J. Geophys. Res.*, 107(B9), 2193, doi:10.1029/2001jb000576.

- Swenson, S., and J. Wahr, 2006, Post-processing removal of correlated errors in GRACE data, *Geophys. Res. Lett.*, *33*, L08402, doi: 10.1029/2005gl025285.
- Swenson, S., D. Chambers, and J. Wahr, 2008, Estimating geocenter variations from a combination of GRACE and ocean model output, *Journal of Geophysical Research: Solid Earth*, *113*, B08410, doi: 10.1029/2007JB005338.
- Syed, T. H., J. S. Famiglietti, J. Chen, M. Rodell, S. I. Seneviratne, P. Viterbo, and C. R. Wilson, 2005, Total basin discharge for the Amazon and Mississippi River basins from GRACE and a land-atmosphere water balance, *Geophys. Res. Lett.*, *32*, L24404, doi: 10.1029/2005gl024851.
- Tamisiea, M. E., J. X. Mitrovica, and J. L. Davis, 2007, GRACE gravity data constrain ancient ice geometries and continental dynamics over Laurentia, *Science*, *316*(5826), 881–883, doi:10.1126/science.1137157.
- van den Broeke, M., J. Bamber, J. Ettema, E. Rignot, E. Schrama, W. J. van de Berg, E. van Meijgaard, I. Velicogna, and B. Wouters, 2009, Partitioning recent Greenland mass loss, *Science*, *326*(5955), 984–986, 10.1126/science.1178176.
- Velicogna, I., and J. Wahr, 2005, Greenland mass balance from GRACE, *Geophysical Research Letters*, *32*, L18505, doi:10.1029/2005GL023955.
- Velicogna, I., and J. Wahr, 2013, Time-variable gravity observations of ice sheet mass balance: Precision and limitations of the GRACE

satellite data, *Geophysical Research Letters*, 40(12), 3055–3063, doi: 10.1002/grl.50527.

Wahr, J., M. Molenaar, and F. Bryan, 1998, Time variability of the Earth's gravity field: Hydrological and oceanic effects and their possible detection using GRACE, *J. Geophys. Res.*, 103(B12), 30205–30229, doi:10.1029/98jb02844.

Wahr, J., S. Swenson, and I. Velicogna, 2006, Accuracy of GRACE mass estimates, *Geophysical Research Letters*, 33(6), doi: 10.1029/2005GL025305.

Weare, B. C., and J. S. Nasstrom, 1982, Examples of extended empirical orthogonal function analyses, *Monthly Weather Review*, 110(6), 481–485, doi:10.1175/1520-0493.

Wouters, B., and E. J. O. Schrama, 2007, Improved accuracy of GRACE gravity solutions through empirical orthogonal function filtering of spherical harmonics, *Geophys. Res. Lett.*, 34, L23711, doi: 10.1029/2007gl032098.

Wouters, B., D. Chambers, and E. J. O. Schrama, 2008, GRACE observes small-scale mass loss in Greenland, *Geophysical Research Letters*, 35, L20501, doi:10.1029/2008GL034816.

Wouters, B., J. L. Bamber, M. R. van den Broeke, J. T. M. Lenaerts, and I. Sasgen, 2013, Limits in detecting acceleration of ice sheet mass loss due to climate variability, *Nature Geosci.*, 6(8), 613–616, doi: 10.1038/ngeo1874.

- Xu, K., J. Zhang, M. Watanabe, and C. Sun, 2004, Estimating river discharge from very high-resolution satellite data: A case study in the Yangtze River, China, *Hydrological Processes*, 18(10), 1927–1939, doi: 10.1002/hyp.1458.
- Yoon, J.-H., and N. Zeng, 2010, An Atlantic influence on Amazon rainfall, *Climate Dynamics*, 34(2-3), 249–264, doi:10.1007/s00382-009-0551-6.
- Zakharova, E. A., A. V. Kouraev, A. Cazenave, and F. Seyler, 2006, Amazon River discharge estimated from TOPEX/Poseidon altimetry, *Comptes Rendus Geoscience*, 338(3), 188 – 196, doi: 10.1016/j.crte.2005.10.003.
- Zeng, N., J.-H. Yoon, J. A. Marengo, A. Subramaniam, C. A. Nobre, A. Mariotti, and J. D. Neelin, 2008, Causes and impacts of the 2005 Amazon drought, *Environmental Research Letters*, 3, 014002.
- Zwally, H. J., L. Jun, A. C. Brenner, M. Beckley, H. G. Cornejo, J. Dimarzio, M. B. Giovinetto, T. A. Neumann, J. Robbins, J. L. Saba, Y. Donghui, and W. Wang, 2011, Greenland ice sheet mass balance: distribution of increased mass loss with climate warming; 2003-07 versus 1992-2002, *Journal of Glaciology*, 57(201), 88–102, doi: 10.3189/002214311795306682.

국문요약

위성 중력계를 활용한 아마존과 그린랜드 표면 질량의 공간-시간적 재분포 연구

서울대학교 대학원
과학교육과 지구과학 전공
엄 주 영

그레이스(Gravity Recovery and Climate Experiment, GRACE)는 2002년 3월 발사된 이래로 현재까지 한 달 간격으로 지구의 중력장을 관측하고 있다. 이렇게 관측된 중력은 시간과 공간에 대한 변화를 보이는데, 이는 해양, 대기 그리고 육상 사이의 물 순환과 같은 지표 질량의 재배치와 밀접하게 관련되어 있다. 이러한 변화 중 조수(tide)나 해양 동력학, 대기압과 관련된 신호들은 수치 모델에 의해 제거되기 때문에 그레이스 자료에는 이들의 영향이 포함되지 않은 것으로 간주된다. 그러나 이 때 사용된 수치 모델들의 불완전성으로 인해 그레이스 자료에는 미처 제거되지 못한 중력 효과가 포함되어 있다. 특히 한 달 미만의 중력 변동은 모델을 통한 제거가 제한적이기 때문에 경선(longitudinal) 방향의 특이한 띠 무늬를 보이는 알리아싱(aliasing) 에러를 일으킨다. 따라서 이러한 에러들을 제거하여 신호의 손실 없이 지표 질량의 변화를 재현해내는 것은 그레이스 자료의 처리에 있어서 매우 중요한 관심사이며, 대상 연구 지역의 공간 스케일이 작아질수록 이러한 에러 처리는 그 결과에 많은 영향을 미친다.

본 학위 논문에서는 경험직교함수(Empirical Orthogonal Functions, EOF)를 사용하여 아마존강과 그린랜드 빙상의 질량 변화 신호들을 그레이스 에러와 분리하였다. 이들 지역은 기후와 지형적인 특성이 서로 다르기 때문에, 시간과 공간에 대하여 뚜렷이 구분되는 그레이스 자료가 관측된다. 따라서

신호와 에러의 서로 다른 특성들을 고려하기 위해 각 지역에 적합한 수정된 경험직교 함수가 적용되었다. 본 연구에서는 아마존과 그린랜드 지역에 대해 각각 회전 경험직교 함수(rotated EOF)와 확장 경험직교 함수(extended EOF)에 기반하여 새로운 자료 처리 기법을 개발하였다. 아마존 지역에서는 본류를 따라 흐르는 물의 질량 변동을 관측하여 배수량을 추정하였다. 이를 위해 본류에 한정된 육상 물 저장량(Terrestrial Water Storage, TWS) 신호를 그레이스 에러와 분리하는 동시에 인접 지역의 TWS 신호와 성공적으로 구분해 내었다. 그린랜드 지역에서는 질량 변동과 관련된 신호를 알리아싱 에러로부터 분리함으로써 상세한 월간 얼음 질량의 변동을 재현하였다.

아마존 오비도스(Óbidos) 지역에 대한 회전 경험직교함수를 적용하여 해당 분지를 통해 빠져나가는 배수량을 성공적으로 추정하였다. 회전 경험직교함수를 통해 얻어진 시계열은 지상에서 관측한 실제 배수량 자료와 높은 정확도로 일치하지만 수위가 높은 시기에는 그레이스 추정값이 지상 관측보다 일반적으로 큰 수치를 보인다. 이러한 차이는 그레이스가 채널을 따라 흐르는 물의 총량을 측정하는 반면, 지상관측의 경우 홍수 시기에 관측소를 우회하는 수량이 결측되기 때문인 것으로 추정된다. 이러한 결과를 바탕으로 회전 경험직교함수를 아마존 분지 전체로 확장할 수 있었고, 지금까지 지상관측소가 설치되지 않아 관측되지 않았던 아마존 분지 전체의 배수량을 추정할 수 있게 되었다.

그린랜드에 대한 확장 경험함수의 적용은 일반적인 공간 필터들에 비해 훨씬 개선된 그린랜드 빙상의 시간적, 공간적 질량 변동 제공한다. 특히 그린랜드의 질량 변화가 빙상의 표면 질량 평형 (surface mass balance, SMB)에 의해 결정되는 겨울철동안, 확장 경험함수의 결과는 이 지역의 기후 모델과 잘 일치하였다. 이 사실에 기반하여 그레이스 관측 자료와 기후 모델을 해안가 지역의 빙하 유출량을 계산하는 데 사용하였다. 이 결과는 그 크기와

공간적인 분포에 있어서 얼음두께와 빙하 표면 속도 자료를 통해 독립적으로 추정된 결과와 높은 정확도로 일치하였다.

주요어: 그레이스, 경험직교함수, 아마존, 그린랜드, 배수량, 얼음질량변동
학 번: 2007-30920